

# A singlet scalar assisted $N_2$ Leptogenesis and Pseudo-Scalar Dark Matter

Dilip Kumar Ghosh,<sup>1,\*</sup> Purusottam Ghosh,<sup>2,3,†</sup>

Koustav Mukherjee,<sup>1,‡</sup> and Nimmala Narendra<sup>1,§</sup>

<sup>1</sup>*School of Physical Sciences, Indian Association for  
the Cultivation of Science, Kolkata-700032, India*

<sup>2</sup>*Institute of Mathematical Sciences, Taramani, Chennai 600 113, India*

<sup>3</sup>*Homi Bhabha National Institute, Anushakti Nagar, Mumbai 400094, India*

## Abstract

We study the Leptogenesis and Dark Matter in the presence of an extra singlet complex scalar field in an extended discrete  $\mathcal{Z}_3$  symmetry. The vacuum expectation value of the new scalar spontaneously breaks the  $\mathcal{Z}_3$  symmetry. A remnant CP-like  $\mathcal{Z}_2$  symmetry stabilizes the imaginary part of the complex scalar field which can act as a pseudo-Goldstone DM. The real part of the complex scalar couples to RHN opens up new decay channels which can lead to a larger CP-violation in generating the lepton asymmetry. Thus the singlet complex scalar plays a crucial role in understanding the Leptogenesis and Dark Matter parameter space. This singlet complex scalar is also responsible for the First-Order Phase Transition (FOPT) which may provide observable stochastic Gravitational wave signatures. We discuss the possible correlations among these three phenomena.

---

\*Electronic address: [dilipghoshjal@gmail.com](mailto:dilipghoshjal@gmail.com)

†Electronic address: [pghoshiitg@gmail.com](mailto:pghoshiitg@gmail.com)

‡Electronic address: [koustav.physics1995@gmail.com](mailto:koustav.physics1995@gmail.com)

§Electronic address: [nimmalanarendra@gmail.com](mailto:nimmalanarendra@gmail.com)

## I. INTRODUCTION

Cosmological observations indicate that the observable Universe is made of baryonic matter but almost no antimatter. This asymmetry between matter and antimatter of the Universe can be expressed in terms of the baryon-to-photon ratio  $\eta_B = \frac{n_B - \bar{n}_B}{n_\gamma} = (6.09 \pm 0.06) \times 10^{-10}$  [1]. To generate such an asymmetry of the Universe, Sakharov identified three essential conditions in 1967 [2]. They are Baryon number violations, C and CP violations, and departure from thermal equilibrium. The Standard Model (SM) intrinsically permits baryon number violation through non-perturbative effects. Additionally, the Cabibbo-Kobayashi-Maskawa (CKM) matrix incorporates a complex phase, providing a source of CP violation. However, the magnitude of these SM-induced effects is insufficient to generate the observed baryon asymmetry of the Universe. Moreover, in the SM with Higgs mass  $m_H = 125$  GeV, the electroweak phase transition is characterized as cross-over in nature, unable to generate the required out-of-equilibrium conditions needed to satisfy the Sakharov criteria for baryogenesis. Therefore, it is natural, to look for the physics beyond the standard model (BSM) to explain the observed baryon asymmetry in our Universe [3, 4].

Leptogenesis is an attractive mechanism to generate such cosmological Baryon asymmetry of the Universe [5]. Once the lepton asymmetry is generated a portion of it converts to Baryon Asymmetry of the Universe (BAU) via Electroweak sphaleron processes [6]. Leptogenesis got special attention ever since the evidence of non-zero neutrino masses [7–10]. In this mechanism, the heavy right-handed neutrinos that couple to SM particles through the Dirac Yukawa interaction are also responsible for the origin of non-zero neutrino masses via the Type-I Seesaw mechanism [11–13].

Another long-standing puzzle that appears in cosmological evolution is the Dark Matter (DM). The existence of DM is supported by several astrophysical and cosmological observations based on its Gravitational interaction, including the anisotropy of the cosmic microwave background (CMB), Gravitational lensing, and rotational curves of galaxies in the galaxy cluster [14, 15], etc. Analysis of anisotropies in CMB data reveals that approximately one-fourth of the Universe consists of DM, which is non-baryonic and non-luminous [16]. Based on CMB observation, the PLANCK collaboration reported the observed relic density of Dark Matter to be  $\Omega_{\text{DM}} h^2 = 0.120 \pm 0.001$  [1]. However, the nature of DM, its non-Gravitational interactions, and its production mechanism remain unknown. Over the years, different types of production mechanisms of DM in the early Universe have been proposed based on its interaction strength with the visible sector. The WIMP (Weakly Interacting Massive Particle) like DM scenarios are widely studied in the literature [17]. WIMPs are assumed to be in thermal equilibrium with the

visible sector particles in the early Universe at a temperature above its mass scale. The WIMP freezes out from the thermal bath as the Universe expands and the temperature falls below its mass scale. The sizeable interaction with the visible sector enables WIMPs to be detected through Direct (XENON1T[18], PANDAX 4T[19], LZ 2022 [20], etc.), Indirect (FERMI LAT, MAGIC [21, 22]), and collider (LHC, ILC, etc. [23]) search experiments. The non-observation of DM in these experiments imposes constraints on WIMP-like scenarios.

In the seesaw mechanism, the explanation behind the light neutrino masses requires a high energy scale for the right-handed neutrinos that are presently beyond the reach of current or near-future collider experiments. Several attempts have been made in the literature to bring down this scale which are Akhmedov-Rubakov-Smirnov (ARS) mechanism[24], Resonant Leptogenesis [25], Leptogenesis in the scotogenic model of radiative neutrino masses [26, 27], *etc.* In recent work, [28], authors considered a simple real scalar extension claiming the right-handed neutrino mass below the TeV scale so that they can be searched at present and future colliders. For the first time, the general mechanism has been defined in [29]. A real singlet scalar can couple to a pair of right-handed neutrinos. The corresponding new coupling allows new decay channels leading to a larger CP violation. Thus, the lowest right-handed neutrino mass can be brought to a TeV scale. The Leptogenesis parameter space can be expressed in low energy parameters using the Casas-Ibarra parametrization [30]. The advantage of this mechanism is that it can evade the lower bound (Davidson-Ibarra bound [31]) on the lowest right-handed neutrino mass. Here we consider a complex singlet scalar instead of a real scalar, once it gets a vacuum expectation value (vev), the real part of the scalar can play a role in achieving the Leptogenesis as discussed above. The imaginary part of the scalar can act as a Pseudo-scalar Dark Matter candidate under a certain symmetry we impose that can stabilize the Dark Matter. This allows us to explore the study of Leptogenesis and Dark Matter simultaneously within a unified framework, while also facilitating the realization of Leptogenesis at the TeV scale.

In the present work, we consider a simple scenario that extends the SM symmetry with a discrete  $\mathcal{Z}_3$  symmetry and the minimal particle content with two right-handed neutrinos  $N_{1,2}$  and a singlet complex scalar. With this minimal setup, we study the  $N_2$ -Leptogenesis [28, 29, 32] in the presence of a viable Pseudo-scalar Dark Matter. We do not consider the flavor effects for simplicity. The singlet scalar we introduce plays a key role in understanding both the phenomenological concepts: Baryon asymmetry of the Universe and Relic density of Dark Matter. The singlet scalar that couples with the right-handed neutrinos allows the additional contribution to the total CP-asymmetry after it gets a vev. The CP-odd state of the singlet scalar acts as a pseudo-scalar Dark Matter candidate of the model due to a discrete  $\mathcal{Z}_2$  like symmetry of the potential. The CP even state mixes with Standard Model Higgs and

allows the annihilation of Dark Matter to Standard Model particles in addressing the observed relic density of Dark Matter. The quartic coupling of the singlet scalar and SM Higgs, and the vev of the singlet scalar play a crucial role together in both Leptogenesis and Dark Matter sectors. Thus, this model establishes a common parameter space that can be explored through Higgs searches and Dark Matter Direct Detection (DD) experiments and upcoming collider experiments.

The groundbreaking discovery of Gravitational Waves (GW) by the (LIGO)[33] has ushered in a new era of cosmological exploration. Stochastic Gravitational waves, generated during the early Universe, can arise from the strong first-order phase transitions (SFOPT). In our current theoretical framework, the introduction of an additional scalar field coupled to the Standard Model Higgs boson enhances the possibility of such a phase transition. We investigate the parameter space of this extended model that is consistent with both leptogenesis and dark matter phenomena while allowing for a strong first-order phase transition. The inclusion of the  $\mu_3$  term in the scalar potential introduces a barrier in the tree-level potential, facilitating the occurrence of the phase transition. These transitions could produce Gravitational waves that may be detectable by future Gravitational wave observatories like LISA[34], LIGO[33], BBO[35], DECIGO[36], *etc.* Studies related to the FOPT of the  $\mathcal{Z}_3$  model have already been discussed in the literature [37]. The FOPT and GW spectrum studies have been conducted with  $\mathcal{Z}_3$  symmetry in a pNGB dark matter model [38]. Motivated by the above studies, our primary goal in this analysis is to identify a unified parameter space that can simultaneously support low-scale Leptogenesis and a strong first-order phase transition, while meeting all current dark matter constraints. To illustrate the SFOPT phenomenon and its potential observable signatures of stochastic Gravitational waves, we select a few representative benchmark points that comply with theoretical and existing experimental constraints. Our analysis demonstrates that the SFOPT primarily driven by the Standard Model Higgs boson is highly improbable in this parameter space, even in scenarios with under-abundant dark matter relic densities, discussed in Sec.VI, for benchmark points BP 1 and BP 2. We observe that for BP 1 and BP 2, even though DM relic density, direct and indirect searches satisfy the current experimental reaches, the value of  $\eta_B$  is large to satisfy the BAU. However, we will show that SFOPT driven by BSM Higgs bosons remains viable, as evidenced by benchmark points BP 3 and BP 4.

The paper is organized as follows. In Sec.II, we introduce the model and discuss the scalar sector of the model. In Sec.III we discuss the  $N_2$ -Leptogenesis and its parameter space in the presence of a singlet scalar. The Dark Matter relic density and its detection at Direct Detection experiments are discussed in Sec.IV. In Sec.V we examine the strong first-order phase transition (FOPT), which results in the generation of gravitational waves, as discussed in detail in Sec.

V A. In Sec.VI we discuss and analyse our results. Finally, we summarize and conclude in Sec.VII.

## II. THE MODEL

We consider the Standard Model with an extra complex singlet scalar  $\Phi$  and two right-handed neutrinos (RHN)  $N'_i$ , ( $i = 1, 2$ ) under an extended discrete symmetry  $\mathcal{Z}_3$  [38, 39]. Note the  $\mathcal{Z}_3$  transformation leaves the SM fields unchanged. The complex scalar couples with right-handed neutrinos via a dimension-five operator, given in Eq.1. The assigned charges of the new particle content under the  $\mathcal{Z}_3$  symmetry are described in Table I.

Fields	$SU(2)_L$	$U(1)_Y$	$\mathcal{Z}_3$
$N'$	1	0	$N' \rightarrow N'$
$\Phi$	1	0	$\Phi \rightarrow e^{i2\pi/3} \Phi$

TABLE I: Charge assignment of the content of the additional fields under the gauge group  $G_{\text{SM}} \otimes \mathcal{Z}_3$ .

The relevant interaction Lagrangian under the extended gauge group can be written as

$$\mathcal{L} \supset - \left[ \lambda'_{\alpha i} \overline{L_\alpha} \tilde{H} N'_i + \frac{1}{2} (M'_{ij} + \frac{y'_{ij}}{\Lambda} \Phi^\dagger \Phi) \overline{N'_i} N'_j + h.c. \right] - V(H, \Phi), \quad (1)$$

where  $\lambda'_{\alpha i}$  denote the RHN-lepton-Higgs Yukawa matrix with  $\{\alpha = e, \mu, \tau\}$  and  $\{i = 1, 2\}$ .  $L_\alpha = \begin{pmatrix} \nu_\alpha \\ \alpha_L \end{pmatrix}$  denotes the three SM left handed charged lepton doublets and  $\tilde{H} = i\tau H^*$  where  $H$  is the standard model Higgs doublet.  $M'_{ij}$  and  $y'_{ij}$  denote the mass matrix and the coefficient of the dim-5 operator of the neutrinos in the unphysical basis. The scale  $\Lambda$  is the cut-off scale of the model. The scalar potential  $V(H, \Phi)$  reads as

$$V(H, \Phi) = -\mu_H^2 (H^\dagger H) + \lambda_H (H^\dagger H)^2 - \mu_\Phi^2 (\Phi^\dagger \Phi) + \lambda_\Phi (\Phi^\dagger \Phi)^2 + \lambda_{H\Phi} (\Phi^\dagger \Phi) (H^\dagger H) + \frac{\mu_3}{2} (\Phi^3 + \Phi^{\dagger 3}). \quad (2)$$

Note the potential has a  $U(1)_G$  global symmetry and it has a soft breaking term of  $U(1)_G$ , the  $\mu_3$  term, in the absence of which the CP odd state of  $\Phi$ , denoted by  $\chi$ , would be massless after the explicit breaking of  $U(1)_G$ . As  $\Phi$  gets a vev,  $\mathcal{Z}_3$  has broken spontaneously. Even though the  $\mathcal{Z}_3$  has broken the Lagrangian still holds a  $\Phi \rightarrow \Phi^\dagger$  symmetry (which is equivalent to  $\chi \rightarrow -\chi$ ) due to which the  $\chi$  is stable [38]. Therefore,  $\mathcal{Z}_2$  is the remnant discrete symmetry under which  $\chi$  transforms non-trivially, while the other fields remain unchanged. The real component of the complex scalar field  $\Phi$  acquires nonzero vev  $v_\phi$  (at high temperature  $T_\Phi \gg T_{EW}$ ) along the CP

even field direction and the  $\Phi$  field can be expanded around the vev as

$$\Phi = \frac{1}{\sqrt{2}}(\phi + v_\phi + i\chi).$$

Both the CP-even and CP-odd states of  $\Phi$  acquire non-degenerate masses, given by

$$M_\phi^2 = 2\lambda_\Phi v_\phi^2 + \frac{3\mu_3 v_\phi}{2\sqrt{2}} \quad \text{and} \quad M_\chi^2 = -\frac{9\mu_3 v_\phi}{2\sqrt{2}}. \quad (3)$$

The right-handed neutrino mass matrix  $M'_{ij}$  receives additional contribution from the vev ( $v_\phi$ ) of  $\Phi$ , *i.e.*, ( $M'_{ij} + v_\phi^2 y'_{ij}/(2\Lambda)$ ). After diagonalizing, the relevant Lagrangian can be written as:

$$-\mathcal{L} \supset \left[ \lambda_{\alpha i} \bar{L}_\alpha \tilde{H} N_i + \frac{1}{2} (D_N)_{ij} \bar{N}_i^c N_j + \alpha_{ij} \phi \bar{N}_i^c N_j + h.c. \right] + V(H, \phi), \quad (4)$$

where  $D_N \equiv \text{diag}(M_{N_1}, M_{N_2})$  is the mass matrix of the right-handed neutrinos in their physical basis. Here, the dimensionless variable  $\alpha_{ij}$  represents the strength of the trilinear interaction term:  $\phi \bar{N}_i^c N_j$ . The  $\alpha_{ij}$  is a complex symmetric matrix because of the Majorana nature of the right-handed neutrinos. The  $(D_N)_{ij}$  and  $\alpha_{ij}$  do not diagonalize simultaneously which allows flavor-changing neutral current interactions among the right-handed neutrinos. Both these two terms violate global lepton number.

After Electroweak Symmetry Breaking (EWSB) (the scale is substantially lower than the  $\mathcal{Z}_3$  breaking scale), the SM Higgs doublet gets non-zero vev along the CP even direction. The Higgs around the EW vev ( $v \simeq 246$  GeV) can be parameterized as,

$$H = \begin{pmatrix} 0 \\ \frac{1}{\sqrt{2}}(h + v) \end{pmatrix}.$$

After EWSB, the low-energy Lagrangian obtains the following form [28]:

$$-\mathcal{L} \supset \left[ \lambda_{\alpha i} \nu_\alpha N_i \left( \frac{v+h}{\sqrt{2}} \right) + \frac{1}{2} (D_N)_{ij} \bar{N}_i^c N_j + \alpha_{ij} \phi \bar{N}_i^c N_j + h.c. \right] + V(h, \phi), \quad (5)$$

This Lagrangian leads us to the Type-I Seesaw mechanism.

Minimizing the scalar potential  $V(H, \Phi)$  at the vacuums ( $v$  and  $v_\phi$ ), one can obtain the following relations,

$$\begin{aligned} \mu_H^2 &= \lambda_H v^2 + \frac{\lambda_{H\Phi} v_\phi^2}{2}, \\ \mu_\Phi^2 &= \lambda_\Phi v_\phi^2 + \frac{\lambda_{H\Phi} v^2}{2} + \frac{3\mu_3 v_\phi}{2\sqrt{2}}. \end{aligned} \quad (6)$$

The two CP even (CPE) states  $h$  and  $\phi$  are mixed up after the EWSB and the mass matrix reads as,

$$\mathcal{M}_{\text{CPE}}^2 = \begin{pmatrix} 2\lambda_H v^2 & \lambda_{H\Phi} v v_\phi \\ \lambda_{H\Phi} v v_\phi & 2\lambda_\Phi v_\phi^2 + \frac{3\sqrt{2}}{4} v_\phi \mu_3 \end{pmatrix} = \begin{pmatrix} A & C \\ C & B \end{pmatrix}. \quad (7)$$

The eigenvalues of the aforementioned mass matrix associated with the two physical states  $h_1$  and  $h_2$  are as follows:

$$M_{h_1, h_2} = \frac{1}{2} \left( (A + B) \mp \sqrt{(A - B)^2 + 4C^2} \right). \quad (8)$$

The mass eigenstates  $h_1$  and  $h_2$  are related to the flavor states  $h$  and  $\phi$  through the following orthogonal transformation, parameterized by the mixing angle  $\theta$  :

$$\begin{pmatrix} h_1 \\ h_2 \end{pmatrix} = \begin{pmatrix} \cos \theta & -\sin \theta \\ \sin \theta & \cos \theta \end{pmatrix} \begin{pmatrix} h \\ \phi \end{pmatrix} \quad \text{with} \quad \tan 2\theta = \frac{2C}{A - B}. \quad (9)$$

Here  $h_1$  is identified as the SM-like Higgs with mass  $M_{h_1} \simeq 125$  GeV and  $h_2$  is the beyond the SM (BSM) scalar with a mass denoted as  $M_{h_2}$ . In the complete alignment limit, ( $\sin \theta \approx 0$ ) the physical states  $h_1$  and  $h_2$  can be identified as the pure SM Higgs boson ( $h_{\text{SM}}$ ) and one singlet state  $\phi$ , with masses  $M_{h_{\text{SM}}}$  and  $M_\phi$  respectively.

Following the above relations, we can express the quartic and cubic couplings in terms of various measurable physical quantities : heavy scalar masses ( $M_{h_1}, M_{h_2}, M_\chi$ ), vev's ( $v, v_\phi$ ) and the scalar mixing angle ( $\sin \theta$ ). The relations are as follows:

$$\begin{aligned} \lambda_H &= \frac{1}{2v^2} (M_{h_1}^2 \cos^2 \theta + M_{h_2}^2 \sin^2 \theta), \\ \lambda_\Phi &= \frac{1}{2v_\phi^2} \left( M_{h_2}^2 \cos^2 \theta + M_{h_1}^2 \sin^2 \theta + \frac{1}{3} M_\chi^2 \right), \\ \lambda_{H\Phi} &= \frac{1}{v v_\phi} (M_{h_2}^2 - M_{h_1}^2) \cos \theta \sin \theta, \\ \mu_3 &= -\frac{2\sqrt{2}}{9} \frac{M_\chi^2}{v_\phi}. \end{aligned} \quad (10)$$

The phenomena of Leptogenesis, the Electroweak phase transition, and Dark Matter production via the freeze-out mechanism depend on the thermal history of the Universe, which we will explore in our discussion. The phenomenon of Leptogenesis occurs at high temperatures ( $T_\Phi > T > T_{\text{EW}}$ )<sup>1</sup>. Contrarily, the Dark Matter maintains thermal equilibrium even after the EWSB phase, *i.e.*, at a temperature around  $T_{\text{FO}} \sim \frac{M_\chi}{3} < T_{\text{EW}}$ . The phenomenology of the model depends on the following independent parameters:

$$\begin{aligned} &\{M_\phi, v_\phi, M_{N_{1,2}}, \alpha_{ij}\} && \text{for Leptogenesis} \\ \text{and } &\{M_{h_2}, M_\chi, v_\phi, \sin \theta\} && \text{for Dark Matter.} \end{aligned} \quad (11)$$

---

<sup>1</sup> The generated lepton asymmetry transfers to the baryon asymmetry through EW sphaleron processes. The baryon asymmetry is conserved after the EW sphaleron processes decouple from the thermal bath at a temperature ( $T_{\text{sph}} \sim 10^2$ ) GeV.

In our discussion of DM, we consider that the right-handed neutrino masses ( $M_{N_{1,2}}$ ) are much heavier than the DM mass  $M_\chi$ . Therefore,  $M_{N_{1,2}}$  will not appear in the DM analysis. The mass parameter  $M_\phi$ , which represents the mass of the  $\phi$  state prior to the electroweak symmetry breaking (EWSB), is related to the mass parameter  $M_{h_2}$ , corresponding to the mass of the physical state  $h_2$  in the following manner:

$$M_\phi^2 = M_{h_2}^2 \cos^2 \theta + M_{h_1}^2 \sin^2 \theta \xrightarrow{\sin \theta \rightarrow 0} \simeq M_{h_2}^2 . \quad (12)$$

### A. Theoretical and Experimental constraints

#### • Stability of potential:

The quartic terms of the scalar potential  $V(H, \Phi)$  play an important role in ensuring the stability of the potential, followed by the following co-positivity conditions [40]:

$$\lambda_H \geq 0, \quad \lambda_\Phi \geq 0 \quad \text{and} \quad \lambda_{H\Phi} + 2\sqrt{\lambda_H \lambda_\Phi} \geq 0. \quad (13)$$

#### • Perturbative Unitarity:

The quartic couplings of the scalar potential also be constrained from tree-level unitarity of the theory, considering all possible  $2 \rightarrow 2$  scattering amplitudes that contribute to the S matrix [41]. The eigenvalues of the  $S$  matrix are bounded from above as:

$$\begin{aligned} |\lambda_H| < 4\pi, \quad |\lambda_\Phi| < 4\pi, \quad |\lambda_{H\Phi}| < 8\pi \\ |(3\lambda_H + 2\lambda_\Phi) \pm \sqrt{2\lambda_{H\Phi}^2 + (3\lambda_H - 2\lambda_\Phi)^2}| < 8\pi . \end{aligned} \quad (14)$$

#### • Collider constraints:

The presence of the BSM scalar can modify the tree-level interactions of the SM Higgs with other SM particles through the mixing ( $\sin \theta$ ). Combining measurements of different final states ( $\gamma\gamma, \gamma Z, WW, ZZ, bb, \mu\mu, \tau\tau$ ) by ATLAS [42] and CMS [43], the Higgs signal strengths set an upper limit on the mixing angle at 95% CL:  $|\sin \theta| \lesssim 0.29$  [44]. The  $W$  mass correction at NLO imposes the most stringent constraint on the mass range of  $M_{h_2} \sim \{250 - 1000\}$  GeV, with the mixing angle  $\sin \theta \sim \{0.2 - 0.3\}$  [45]. On the other hand, the electroweak precision observables impose weaker constraints on  $\sin \theta$  compared to that obtained from  $W$ -boson mass corrections [45].

If the dark matter (DM) mass is below  $M_{h_1}/2$ , the SM-like Higgs can decay to DM pairs ( $h_1 \rightarrow \chi\chi$ ), contributing to the Higgs invisible decay width. The ATLAS collaboration has placed a strong constraint on the Higgs invisible branching ratio,  $\text{Br}(h_{\text{SM}} \rightarrow \text{inv})$ , setting it below 13% [46]. The Higgs invisible branching ratio can be expressed as (considering  $M_{h_2} >$

$M_{h_1}$ ):

$$\text{Br}(h_1 \rightarrow \text{inv}) = \frac{\sin^2 \theta \Gamma(\phi \rightarrow \chi\chi)}{\sin^2 \theta \Gamma(\phi \rightarrow \chi\chi) + \cos^2 \theta \Gamma(h \rightarrow \text{SM SM})} \quad (15)$$

with  $\Gamma(h \rightarrow \text{SM SM}) \simeq 4.1 \text{ MeV}$ .

### III. LEPTOGENESIS IN PRESENCE OF A SINGLET SCALAR

The additional singlet scalar  $\Phi$  opens up a large CP-violation compared to standard Thermal Leptogenesis in the Type-I seesaw model. Once the  $\Phi$  acquires a vacuum expectation value, the relevant couplings that appear in the Leptogenesis sector can be expressed as:

$$\frac{y'_{ij}}{\Lambda} \Phi^\dagger \Phi \overline{N'_i} N'_j + \lambda_{H\Phi} \Phi^\dagger \Phi H^\dagger H \rightarrow \alpha_{ij} \phi \overline{N_i} N_j + \xi \phi (H^\dagger H), \quad (16)$$

where we define  $\xi = \lambda_{H\Phi} v_\phi$ .

The interference of tree and loop level diagrams gives a non-zero contribution to the CP-asymmetry. In Fig. 1, we show the tree and loop-level (vertex and self-energy) Feynman diagrams for the case of standard Thermal Leptogenesis and the  $N_2$ -Leptogenesis. The additional loop diagrams that appear from the additional interaction terms, given in the third row of Fig. 1, play a crucial role in enhancing the CP violation in the  $N_2$  Leptogenesis scenario<sup>2</sup> [29].

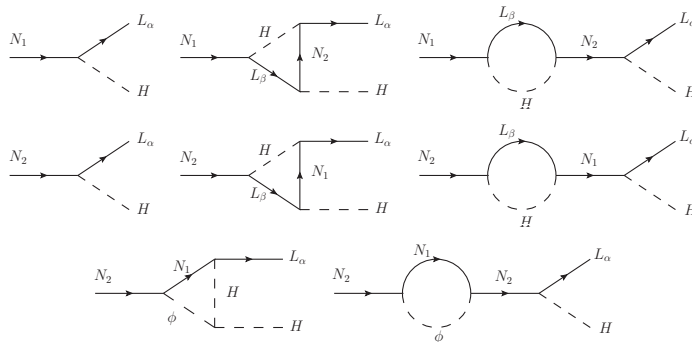


FIG. 1: Contribution of the tree and loop level (vertex and self-energy) diagrams to the total CP asymmetry.

As we mentioned in Sec. II, the Lagrangian given in Eq. 5 sets a stage for the Type-I seesaw mechanism. After integrating out the heavy degrees of freedom, we get the light neutrino mass matrix  $m_\nu$  as the following:

$$m_\nu = -m_D D_N^{-1} m_D^T, \quad (17)$$

where  $m_D = \lambda v / \sqrt{2}$  is the Dirac mass matrix. The light neutrino matrix can be diagonalized by a unitary transformation  $U$  which coincides with PMNS (Pontecorvo-Maki-Nakagawa-Sakata)

<sup>2</sup>  $N_1 \rightarrow N_2 + \phi$  kinematically forbidden since we consider  $M_{N_2} > M_{N_1} + M_\phi$ .

lepton mixing matrix,

$$D_\nu = U^T m_\nu U = \text{diag}(m_1, m_2, m_3). \quad (18)$$

We work in the flavor basis where the charged-lepton Dirac mass matrix is diagonal, and use the Casas-Ibarra parametrization[30] to re-express the neutrino Yukawa coupling matrix  $\lambda$  in terms of low energy parameters as given below:

$$\lambda = \frac{i}{v} U^* D_\nu^{1/2} R D_N^{1/2}, \quad (19)$$

where  $R$  is a complex  $3 \times 2$  orthogonal matrix ( $R^T R = \mathbb{1}$ ) which can be parametrized in terms of one complex angle,  $z'$ . The  $U$  matrix contains three mixing angles ( $\theta_{12}, \theta_{23}$  and  $\theta_{13}$ ), Dirac phase ( $\delta$ ) and Majorana phase ( $\gamma_1$ ). The  $D_\nu$  depends on two mass-squared differences  $\Delta m_{\text{sol}}^2$  and  $\Delta m_{\text{atm}}^2$  in light neutrino mass spectrum[47, 48].

In the standard thermal Leptogenesis, the CP-asymmetry, *i.e.* in the absence of the additional loop diagrams, can be expressed as

$$\epsilon_{i=1,2}^0 = \frac{1}{8\pi(\lambda^\dagger \lambda)_{ii}} \sum_{j \neq i} \text{Im} [(\lambda^\dagger \lambda)_{ji}^2] \mathcal{F} \left( \frac{M_{N_j}}{M_{N_i}} \right), \quad (20)$$

where

$$\mathcal{F}(x) = x \left[ 1 + (1 + x^2) \ln \left( \frac{x^2}{x^2 + 1} \right) - \frac{1}{x^2 - 1} \right]. \quad (21)$$

The CP-asymmetry is the sum of the vertex and self-energy diagrams contribution. For the present case, the total CP-asymmetry is the sum of the contributions that come from the CP-asymmetry in the absence of additional diagrams and the presence of additional diagrams.

$$\epsilon_1 = \epsilon_1^0, \quad \epsilon_2 = \epsilon_2^0 + \epsilon_2^v + \epsilon_2^s \quad (22)$$

where

$$\begin{aligned} \epsilon_2^v &= \frac{1}{8\pi(\lambda^\dagger \lambda)_{22} M_{N_2}} \{ \text{Im} [(\lambda^\dagger \lambda)_{12} \xi \alpha_{21}] \mathcal{F}_{21,R}^v + \text{Im} [(\lambda^\dagger \lambda)_{12} \xi \alpha_{21}^*] \mathcal{F}_{21,L}^v \}, \\ \epsilon_2^s &= \frac{1}{8\pi(\lambda^\dagger \lambda)_{22}} \{ \text{Im} [(\lambda^\dagger \lambda)_{12} \alpha_{21} \alpha_{11}] \mathcal{F}_{211,RR}^s + \text{Im} [(\lambda^\dagger \lambda)_{12} \alpha_{21}^* \alpha_{11}] \mathcal{F}_{211,RL}^s \\ &\quad + \text{Im} [(\lambda^\dagger \lambda)_{12} \alpha_{21} \alpha_{11}^*] \mathcal{F}_{211,LR}^s + \text{Im} [(\lambda^\dagger \lambda)_{12} \alpha_{21}^* \alpha_{11}^*] \mathcal{F}_{211,LL}^s \}. \end{aligned} \quad (23)$$

The explicit expressions for the loop function  $\mathcal{F}$  can be found in Appendix VIII B. We refer [28, 29] for greater details.

To study the evolution of the number densities of the right-handed neutrinos  $N_i$  ( $i = 1, 2$ ) and the amount of  $B - L$  asymmetry  $N_{B-L}$ , we consider a set of coupled Boltzmann equations while taking care of their decay and inverse decay rates and scattering processes. In the present scenario, the decay of  $N_2$  to  $N_1$  and  $\phi$ , (*i.e.*  $N_2 \rightarrow N_1 \phi$ ) and the washout processes *i.e.*,  $\Delta L = 2$

scatterings  $N_i N_j \rightarrow HH$  play a key role in addressing the low scale Leptogenesis. The relevant Boltzmann equations for the number densities  $N_{N_{1,2}}$  and  $N_{B-L}$  can be expressed as [28]

$$\begin{aligned}
\frac{dN_{N_2}}{dz} &= -(D_2 + D_{21}) \left( \frac{N_{N_2}(z)}{N_{N_2}^{\text{eq}}(z)} - 1 \right) + D_{21} \left( \frac{N_{N_1}(z)}{N_{N_1}^{\text{eq}}(z)} - 1 \right) \\
&\quad - S_{N_1 N_2 \rightarrow HH} \left( \frac{N_{N_1} N_{N_2}}{N_{N_1}^{\text{eq}} N_{N_2}^{\text{eq}}} - 1 \right) - S_{N_2 N_2 \rightarrow HH} \left( \frac{N_{N_2} N_{N_2}}{N_{N_2}^{\text{eq}} N_{N_2}^{\text{eq}}} - 1 \right) \\
\frac{dN_{N_1}}{dz} &= -(D_1 + D_{21}) \left( \frac{N_{N_1}(z)}{N_{N_1}^{\text{eq}}(z)} - 1 \right) + D_{21} \left( \frac{N_{N_2}(z)}{N_{N_2}^{\text{eq}}(z)} - 1 \right) \\
&\quad - S_{N_1 N_2 \rightarrow HH} \left( \frac{N_{N_1} N_{N_2}}{N_{N_1}^{\text{eq}} N_{N_2}^{\text{eq}}} - 1 \right) - S_{N_1 N_1 \rightarrow HH} \left( \frac{N_{N_1} N_{N_1}}{N_{N_1}^{\text{eq}} N_{N_1}^{\text{eq}}} - 1 \right) \\
\frac{dN_{B-L}}{dz} &= \epsilon_1 D_1 \left( \frac{N_{N_1}(z)}{N_{N_1}^{\text{eq}}(z)} - 1 \right) + \epsilon_2 D_2 \left( \frac{N_{N_2}(z)}{N_{N_2}^{\text{eq}}(z)} - 1 \right) - (W_1 + W_2) N_{B-L}. \quad (24)
\end{aligned}$$

where the  $z_1 \equiv M_{N_1}/T$  (with  $z \equiv z_1$ ) and  $z_2 \equiv M_{N_2}/T = (M_{N_2}/M_{N_1})z$  are the dimensionless parameters. The  $N_{N_i}^{\text{eq}}$  are the equilibrium number densities,

$$N_{N_i}^{\text{eq}}(z) = \frac{z_i^2}{2} \mathcal{K}_2(z_i). \quad (25)$$

The  $D_{1,2}$ ,  $D_{21}$  and  $W$  are (function of  $z$ ) the decay rate of right-handed neutrinos  $N_{1,2} \rightarrow LH$ ,  $N_2 \rightarrow N_1 \phi$  and washout from the inverse decays  $LH \rightarrow N_{1,2}$ , respectively,

$$D_i(z) = K_i z \frac{\mathcal{K}_1(z_i)}{\mathcal{K}_2(z_i)} N_{N_i}^{\text{eq}}(z), \quad (26)$$

$$D_{21}(z) = K_{21} z \frac{\mathcal{K}_1(z_2)}{\mathcal{K}_2(z_2)} N_{N_2}^{\text{eq}}(z), \quad (27)$$

$$W(z) = \sum_i \frac{1}{4} K_i z_i^3 \mathcal{K}_1(z_i), \quad (28)$$

where  $\mathcal{K}_{1,2}(z)$  are the modified Bessel functions of the second kind. The decay parameters can be expressed as,

$$K_i \equiv \frac{\Gamma(N_i \rightarrow LH)}{\mathcal{H}(T = M_{N_i})}, \quad K_{21} \equiv \frac{\Gamma(N_2 \rightarrow N_1 \phi)}{\mathcal{H}(T = M_{N_2})}, \quad (29)$$

where  $\mathcal{H} = \sqrt{8\pi^3 g_*/90} T^2/M_{\text{pl}}$  is the Hubble rate. The decay widths can be expressed as,

$$\Gamma_i = \Gamma(N_i \rightarrow LH) + \Gamma(N_i \rightarrow \bar{L}\bar{H}) = \frac{(\lambda^\dagger \lambda)_{ii}}{8\pi} M_{N_i}, \quad (30)$$

$$\Gamma(N_2 \rightarrow N_1 \phi) = \frac{|\alpha_{12}|^2 M_{N_2}}{16\pi} \left[ \left( 1 + \frac{M_{N_1}}{M_{N_2}} \right)^2 - \frac{M_\phi^2}{M_{N_2}^2} \right] \sqrt{\left( 1 - \frac{M_{N_1}^2}{M_{N_2}^2} - \frac{M_\phi^2}{M_{N_2}^2} \right)^2 - 4 \frac{M_{N_1}^2}{M_{N_2}^2} \frac{M_\phi^2}{M_{N_2}^2}}. \quad (31)$$

The scattering cross-section function for  $N_i N_j \rightarrow HH$  can be expressed as

$$S_{N_i N_j \rightarrow HH} \equiv \frac{M_{N_i}}{64\pi^2 \mathcal{H}(T = M_{N_i})} \int_{w_{\text{min}}}^{\infty} \sqrt{w} K_1(\sqrt{w}) \hat{\sigma}_{N_i N_j \rightarrow HH} \left( \frac{w M_{N_i}^2}{z_i^2} \right), \quad (32)$$

where  $w_{\min} = (M_{N_i} + M_{N_j})^2$ , and

$$\hat{\sigma} = \frac{1}{s} \delta(s, M_{N_i}, M_{N_j}) \sigma_{N_i N_j \rightarrow HH}, \quad (33)$$

where  $\sigma$  is cross-section for the scatterings  $N_i N_j \rightarrow HH$ ,

$$\sigma(N_i N_j \rightarrow HH) = \frac{|\alpha_{ij}|^2 \xi^2}{32\pi} \frac{s - (M_{N_i} + M_{N_j})^2}{\sqrt{\delta(s, M_{N_i}, M_{N_j})} (s - M_S^2)^2}, \quad (34)$$

with  $\delta(s, M_{N_i}, M_{N_j}) = (s - M_{N_i}^2 - M_{N_j}^2)^2 - 4M_{N_i}^2 M_{N_j}^2$ .

In our scenario, the contribution to the total  $B - L$  asymmetry comes from the decays of both heavy right-handed neutrinos  $N_2$  and  $N_1$ . As the Universe expands and cools down to a temperature  $T \sim M_{N_2}$ , *i.e.*,  $z_2 \sim 1$ , the  $N_2$  decays in its out-of-equilibrium to leptons and Higgs particles and generates the primary lepton asymmetry. In the presence of the new channels,  $N_2$  can also decay to  $N_1$  and  $\phi$  through the coupling  $\alpha_{12}$ . It can increase the abundance of  $N_1$ . Subsequently,  $N_1$  also decays in its out-of-equilibrium around the temperature  $T \sim M_{N_1}$ , *i.e.*,  $z_1 \sim 1$ , analogous to the  $N_2$  decay. Due to the small CP asymmetry, this contribution is very small to the total lepton asymmetry. When  $N_1$  is in equilibrium its inverse decays can wash out the asymmetry that was produced previously from the  $N_2$  decays.

We numerically solve the Boltzmann equations given in Eq.24. We depict the estimated abundances of  $N_1, N_2$  and  $N_{B-L}(\eta_B)$  in Fig.2. In Fig.2 (a), the Blue (dashed) and Orange (dot-dashed) lines show the abundances of  $N_2$  and  $N_1$  respectively.

The generated  $N_{B-L}$  asymmetry obtained from Eq.24, converts into the baryon asymmetry via the induced Sphaleron processes. The predicted  $N_{B-L}$  is related to the  $\eta_B$  measured at recombination given as

$$\eta_B = \left( \frac{a_{sph}}{f} \right) N_{B-L}, \quad (35)$$

where  $a_{sph} = 28/79$  is the fraction of  $B - L$  asymmetry converted into the baryon asymmetry by sphaleron processes, and  $f = N_\gamma^{\text{rec}}/N_\gamma^* = 2387/86$  is the dilution factor calculated assuming standard photon production from the onset of Leptogenesis till recombination [49].

The Green dotted line in Fig.2 shows the abundance of the baryon asymmetry,  $\eta_B$ . We fix the parameters:  $M_{N_2} = 7.5 \times 10^3$  GeV,  $M_{N_1} = 5 \times 10^3$  GeV,  $M_\phi = 500$  GeV,  $\alpha_{ij} = 10^{-3}$ , and  $\xi = 6 \times 10^3$  GeV. In our model,  $\alpha_{ij}$  and  $\xi$  plays a crucial role. We illustrate our results in terms of  $\xi (= \lambda_{H\Phi} v_\phi)$  only, where the  $\lambda_{H\Phi}$  play a key role in DM and FOPT. Whereas  $\alpha_{ij}$  apart from its magnitude, it won't play much phenomenology. As  $\alpha_{ij}$  is a complex matrix, it can be an additional source of CP violation. But for simplicity we avoid it. The CP-violation appears due to  $\lambda_{ij}$ , see Eq.23. The  $\lambda_{ij}$  we can parametrize through Casas-Ibarra parametrization given in Eq.19. Since the  $\alpha_{ij}$  is proportional to CP-asymmetry ( $\epsilon_2$ ), it can maximize the CP-asymmetry but it can also impact the washouts from the scattering processes, given in Eq.34.

For large values of  $\alpha_{ij}$  the CP-asymmetry( $\epsilon$ ) can be large but the washout is also high. It suppresses the RHN abundance and hence the lepton asymmetry. For small values of  $\alpha_{ij}$  the washout may be smaller but the CP-asymmetry is suppressed, hence lepton asymmetry. So we fixed it with appreciable value for  $\alpha_{ij} = 10^{-3}$  to get asymmetry in a reasonable range. Throughout our analysis, we fix the complex angle  $z' = 0.01 + i 0.8$ . The horizontal Gray line represents the observed baryon asymmetry of the Universe. In Fig.2 (b) the Blue(dot-dashed) and Orange(dashed) line shows the deviations ( $\Delta N_i = N_{N_i} - N_{N_i}^{\text{eq}}$ ,  $\{i = 1, 2\}$ ) of the abundance of  $N_1$  and  $N_2$  from their equilibrium abundances. Both plots show a drop in the baryon asymmetry(Green dotted line) caused by the washout processes before becoming constant.

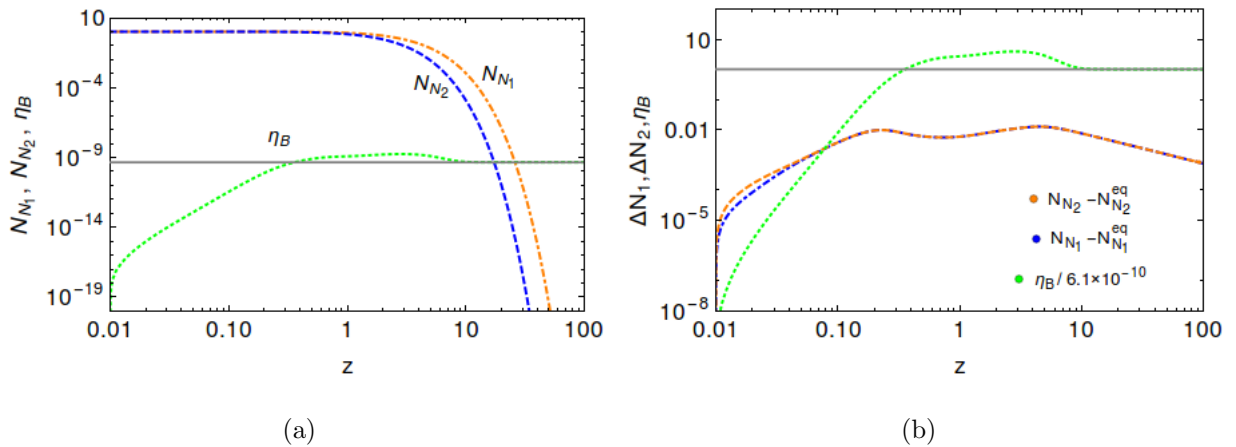


FIG. 2: (a) Variation of the abundances of  $N_2, N_1$  and  $\eta_B$  as a function of variable  $z = M_{N_1}/T$ . (b) Variation of the deviation of  $N_2, N_1$  abundances from their equilibrium abundances as a function of the same variable  $z$ . The Black horizontal line represents the observed baryon asymmetry of the Universe. We fix the parameters as follows:  $M_{N_2} = 7.5 \times 10^3$  GeV,  $M_{N_1} = 5 \times 10^3$  GeV,  $M_\phi = 500$  GeV,  $\alpha_{ij} = 10^{-3}$ , and  $\xi = 6 \times 10^3$  GeV.

In Fig.3 (a), we display the variation of  $\eta_B$  with  $M_\phi$  and  $\xi$ . In Fig.3 (b), we fix the  $\xi = 700$  (Pink – dotted), 800 (Cyan – dotdashed), and 900 (Orange – dashed) GeV and vary  $M_\phi$ . The baryon asymmetry remains relatively constant as the mass of the scalar field,  $M_\phi$  increases until it approaches the mass difference between the heavy neutrinos,  $M_{N_2} - M_{N_1} \sim M_\phi$ . As  $M_\phi$  nears this difference, the decay width  $\Gamma_{21}$  decreases, see Eq.31, leading to a corresponding reduction in baryon asymmetry. This behavior is depicted in Fig.3 (a). In Fig. 3 (b), we illustrate the variation of  $\eta_B$  with  $\xi$ . Here we fix  $M_\phi = 200$  (Red – dotted), 300 (Green – dotdashed), and 400 (Blue – dashed) GeV. Initially, as  $\xi$  increases,  $\eta_B$  rises until it reaches a threshold value  $\xi_{\text{Thres}}$ , beyond which it starts to gradually decrease. Beyond this threshold, scatterings of the form  $N_i N_j \rightarrow HH$  as described in Eq.32 begin to dominate over the decay rates  $D_1, D_2$  and  $D_{21}$ . This dominance leads to an increase in the washout process, suppressing the abundance

of  $N_{1,2}$  causing  $\eta_B$  to decrease. To minimize the washout effects, we confine our analysis to the region where  $\xi < \xi_{\text{Thres}}$ . This ensures that our numerical estimations align well with the analytical predictions, as discussed in [28].

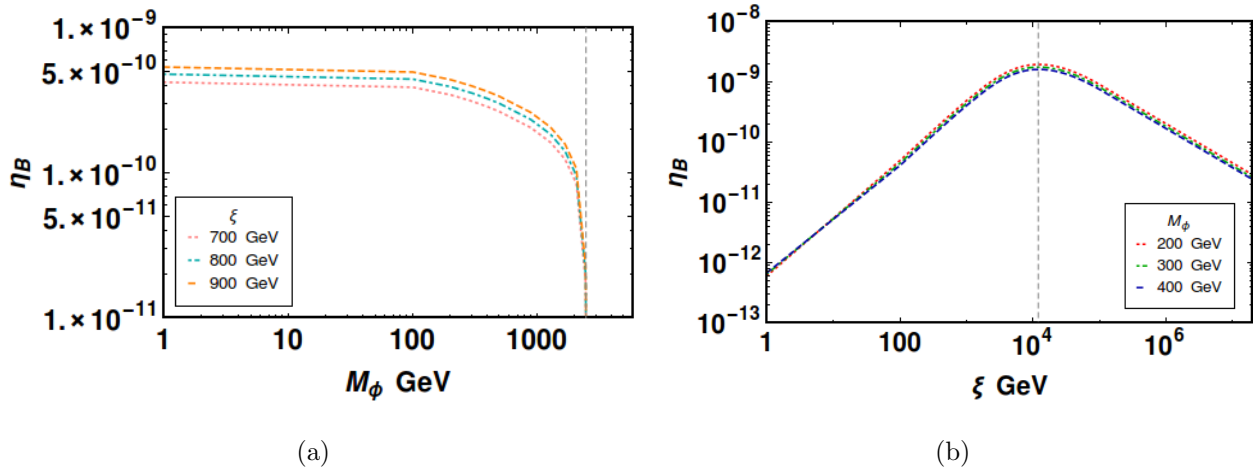


FIG. 3: Figure shows the variation of the baryon asymmetry,  $\eta_B$  with respect to  $M_\phi$  and  $\xi$ . We fix the parameters as follows:  $M_{N_2} = 7.5 \times 10^3$  GeV,  $M_{N_1} = 5 \times 10^3$  GeV and  $\alpha_{ij} = 10^{-3}$ .

In Fig.4, we show the allowed parameter space for the observed baryon asymmetry of the Universe in the plane of  $M_\phi$  and  $\xi$ . The Blue line successfully explains the observed baryon asymmetry of the Universe. The Pink and Blue regions show the under and over-abundant baryon asymmetry, respectively. We consider  $M_{N_2} = 6.5 \times 10^{2,3,4}$  GeV and  $M_{N_1} = 5 \times 10^{2,3,4}$  GeV respectively in Figs. 4 (a), (b), and (c) respectively by keeping  $\delta M = (M_{N_2} - M_{N_1})/M_{N_1} = 0.3$ . Here we show the variation of the baryon asymmetry parameter space in the plane of  $M_\phi$  and  $\xi$  at different mass scales of the right-handed neutrinos. Until  $M_\phi$  value approaches the kinematic limit, the baryon asymmetry remains nearly constant with  $\xi$  to satisfy the observed BAU. Once the  $M_\phi$  reaches near the kinetic limit the baryon asymmetry starts to decrease, hence, the  $\xi$  must increase to get the observed BAU. It continues until  $\xi$  reaches around the threshold  $\xi_{\text{Thres}}$ , the horizontal line. Around the threshold, the washout processes due to scatterings start dominating and reducing the baryon asymmetry. To compensate and achieve the observed BAU, the  $M_\phi$  has to be reduced by keeping  $\xi$  constant. That results in two allowed values for the  $\xi$  with a single value of  $M_\phi$ , see Fig.4 (a). We also notice that as we increase the mass scale of the right-handed neutrinos the allowed  $\xi$  shifts towards larger values, see Fig.4 (b) and (c). In Fig.4 (d), we consider  $\delta M = 0.3, 0.2, 0.1$  corresponding to  $M_{N_2} = (6.5, 6, 5.5) \times 10^4$  GeV and  $M_{N_1} = 5 \times 10^4$  GeV respectively. We see that for a particular mass scale of right-handed neutrinos if we reduce the  $\delta M$  the BAU allowed  $\xi$  decreases.

In the following section, we explore the phenomenology of the Dark Matter. The parameters  $\alpha_{ij}$ ,  $\xi$ , and  $M_\phi(M_{h_2})$  will play a crucial role in determining various characteristic features of the

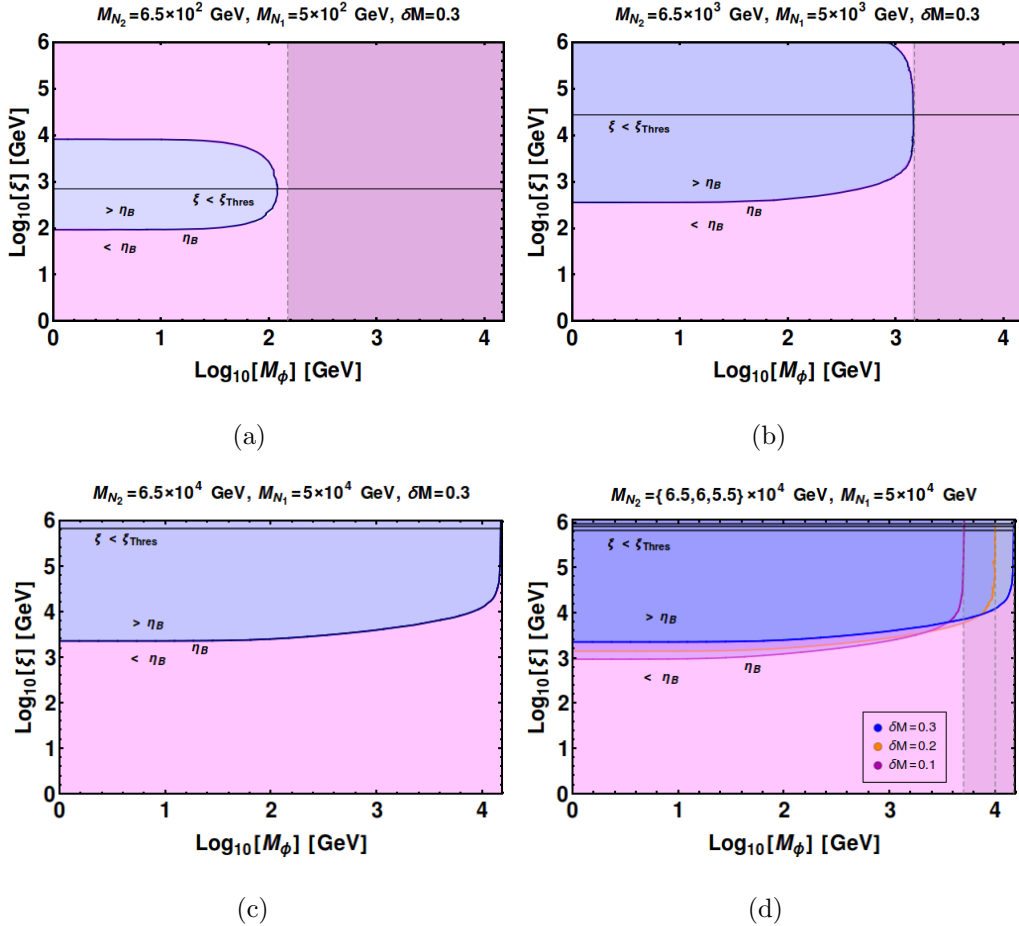


FIG. 4: The behavior of the observed baryon asymmetry of the Universe at different scales,  $M_{N_2} = 6.5 \times 10^{2,3,4}$  GeV with  $\delta M = 0.3$ . We fix  $\alpha_{ij} = 10^{-3}$  to be small to avoid large suppression from scattering processes. The horizontal line corresponds to the threshold limit, where the washout from the scattering rate dominates over the decay rate.

Leptogenesis and the Dark matter and their correlations.

#### IV. PSEUDO SCALAR DARK MATTER PHENOMENOLOGY

This section focuses on the phenomenology of DM  $\chi$ , which is the CP-odd state of the complex singlet scalar  $\Phi$ . The residual  $\Phi \rightarrow \Phi^\dagger$  symmetry ( $\chi \rightarrow -\chi$ ) ensures the stability of DM  $\chi$ . The DM communicates with the visible sector (SM) through the portal interaction  $\lambda_{H\Phi}(H^\dagger H)(\Phi^\dagger \Phi)$ . In the early Universe,  $\chi$  maintained thermal equilibrium with the bath particles through the Higgs portal interaction. This equilibrium condition was determined by the inequality between the interaction rate  $\Gamma_{\text{DM-SM}} \equiv n_\chi^{\text{eq}} \langle \sigma v \rangle_{\chi\chi \rightarrow XY}$  ( $X, Y$  represent the thermal bath particles) and the Hubble expansion rate  $\mathcal{H}$  as  $\Gamma_{\text{DM-SM}} > \mathcal{H}$ . As the Universe expanded, the rate of interaction diminished with decreasing temperature. When the temperature reached a point where  $\Gamma_{\text{DM-SM}}$  went below  $\mathcal{H}$ , DM froze out of the thermal bath, resulting in today's

observed DM density. This phenomenon is referred to as the WIMP (Weakly Interacting Massive Particle) miracle [17]. Note that  $\chi$  maintains thermal equilibrium even after the EWSB at temperatures around  $T_{\text{FO}} \sim M_\chi/20 < T_{\text{EW}}$ . Before DM freezeout ( $T > T_{\text{FO}}$ ), the number density of DM follows the equilibrium density, denoted as  $n_\chi^{\text{eq}}$ . After EWSB, it turns out that the SM Higgs ( $h$ ) and the CP even component of the BSM singlet ( $\phi$ ) mix to form two physical states  $h_1$  (SM-like) and  $h_2$ . Therefore both  $h_1$  and  $h_2$  mediated scattering processes between the DM ( $\chi$ ) and the bath particles ( $X, Y = \{\text{SM}, h_2\}$ ) are responsible for the number density of  $\chi$ . The Feynman diagrams of the number-changing processes of DM are shown in Fig.5 and Fig.6.

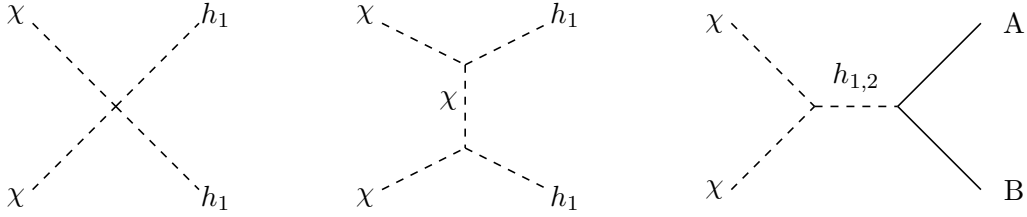


FIG. 5: *Feynmann diagrams for DM annihilation to SM:  $\chi \chi \rightarrow A B$  with  $\{A, B\} = \{W, Z, h_1(M_{h_1} = 125 \text{ GeV}), f(\text{SM fermions})\}$ .*

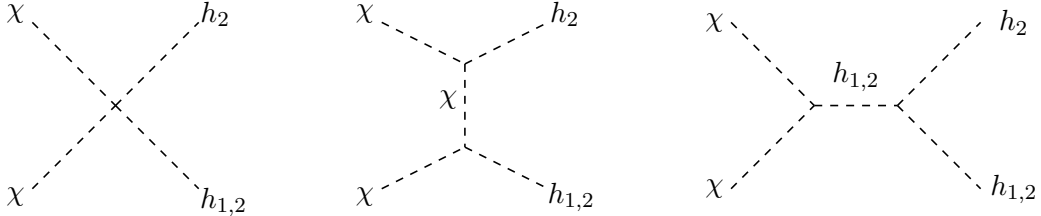


FIG. 6: *Feynmann diagrams for DM annihilation to  $h_{1,2}$ :  $\chi \chi \rightarrow h_2 h_{1,2}$ .*

The evolution of DM number density can be described by solving the Boltzmann equation which is given by [17, 50]:

$$\begin{aligned}
\frac{dn_\chi}{dt} + 3\mathcal{H}n_\chi &= - \sum_{\text{SM}} \langle \sigma v \rangle_{\chi\chi \rightarrow \text{SM}} \text{SM} (n_\chi^2 - n_\chi^{\text{eq}2}) \Theta(M_\chi - M_{\text{SM}}) \\
&\quad - \langle \sigma v \rangle_{\chi\chi \rightarrow h_1 h_2} (n_\chi^2 - n_\chi^{\text{eq}2}) \Theta(2M_\chi - M_{h_1} - M_{h_2}) \\
&\quad - \langle \sigma v \rangle_{\chi\chi \rightarrow h_2 h_2} (n_\chi^2 - n_\chi^{\text{eq}2}) \Theta(M_\chi - M_{h_2}) \\
&= - \langle \sigma v \rangle_{\text{eff}} (n_\chi^2 - n_\chi^{\text{eq}2}).
\end{aligned} \tag{36}$$

Here  $n_\chi^{\text{eq}} = \frac{g_\chi}{2\pi^2} M_\chi^2 T K_2[\frac{M_\chi}{T}]$  [17] is the equilibrium density where  $g_\chi = 1$  and  $K_2$  is the modified Bessel function of the second kind. The  $\langle \sigma v \rangle_{\chi\chi \rightarrow ab}$  is the thermal average cross-section for the

number changing process  $\chi\chi \rightarrow a b$  defined in Ref.[17]. These thermal average annihilation cross-sections of DM depend on the model parameters  $\{M_\chi, M_{h_2}, v_\phi, \sin\theta\}$ . In this thermal freeze-out scenario, the relic density of DM and the total effective thermal-averaged cross-section are related as [17, 50]:

$$\Omega_\chi h^2 \propto \frac{1}{\langle\sigma v\rangle_{\text{eff}}} \quad , \quad (37)$$

where

$$\begin{aligned} \langle\sigma v\rangle_{\text{eff}} = & \sum_{\text{SM}} \langle\sigma v\rangle_{\chi\chi \rightarrow \text{SM}} \Theta(M_\chi - M_{\text{SM}}) + \langle\sigma v\rangle_{\chi\chi \rightarrow h_1 h_2} \Theta(2M_\chi - M_{h_1} - M_{h_2}) \\ & + \langle\sigma v\rangle_{\chi\chi \rightarrow h_2 h_2} \Theta(M_\chi - M_{h_2}). \end{aligned} \quad (38)$$

Here  $\Theta$  is the Heaviside theta function, representing the kinematics of the number-changing process. Depending on DM mass different number-changing processes open up and contribute to the relic density. The approximate relation in Eq.37, will help us to understand the behavior of DM density as a function of model parameters. Note we use the publicly available package MicrOmegas [51] for relic density computation, after generating the model files using FeynRule [52].

In Fig.7, we show the variation of DM relic density ( $\Omega_\chi h^2$ ) as a function of  $M_\chi$  for three different values of  $v_\phi$  in GeV:  $10^2$  (cyan line),  $10^3$  (blue line) and  $10^4$  (red line). For demonstration, we kept fixed  $\sin\theta = 0.1$  in the left panel and  $\sin\theta = 0.01$  in the right panel, and  $M_{h_2} = 400$  GeV for both figures. The black dotted horizontal line in each figure indicates the observed DM relic density measure by PLANCK  $\Omega_\chi h^2 = 0.12$  [1]. As stated earlier the DM connected to the thermal bath particles via the the portal coupling  $\lambda_{H\Phi}$ . Therefore  $\lambda_{H\Phi}$  plays a crucial role in deciding the abundance of DM ( $\Omega_\chi h^2$ ). For a fixed  $M_\chi$  and  $M_{h_2}$ , the portal coupling  $\lambda_{H\Phi}$  varies as:  $\lambda_{H\Phi} \propto \frac{\sin\theta}{v_\phi}$  followed by Eq.10. For a fixed value of  $\sin\theta$ , with an increase in  $v_\phi$ ,  $\lambda_{H\Phi}$  decreases, and as a result,  $\langle\sigma v\rangle_{\text{eff}}$  decreases. Therefore relic density increases with the increase of  $v_\phi$ , as depicted in Fig.7. On the contrary, for a fixed value of  $v_\phi$ , as  $\sin\theta$  decreases,  $\langle\sigma v\rangle_{\text{eff}}$  decreases, increasing relic density. The dependence on  $\sin\theta$  can be understood from the left ( $\sin\theta = 0.1$ ) and right ( $\sin\theta = 0.01$ ) panels of Fig.7 for a fixed value of  $v_\phi$ .

Now we will demonstrate the variation of relic density as a function of DM mass  $M_\chi$ , keeping  $v_\phi, \sin\theta$  and  $M_{h_2}$  constant, thereby fixing the value of  $\lambda_{H\Phi}$ . There are two drops in relic density near  $M_\chi \sim M_{h_1}/2$  ( $\sim 62.5$  GeV) and  $M_{h_2}/2$  ( $\sim 200$  GeV) due to resonance enhancement in the cross-sections around the poles  $h_1$  and  $h_2$  respectively. Depending on  $M_\chi$ , different final states are open up, adding their contribution to  $\langle\sigma v\rangle_{\text{eff}}$ . Therefore, the total effective thermal-averaged cross-section increases with the increase of  $M_\chi$  as followed in Eq.38. Hence relic density drops with the increase of  $M_\chi$ . The active DM annihilation processes vary across different  $M_\chi$  regions,

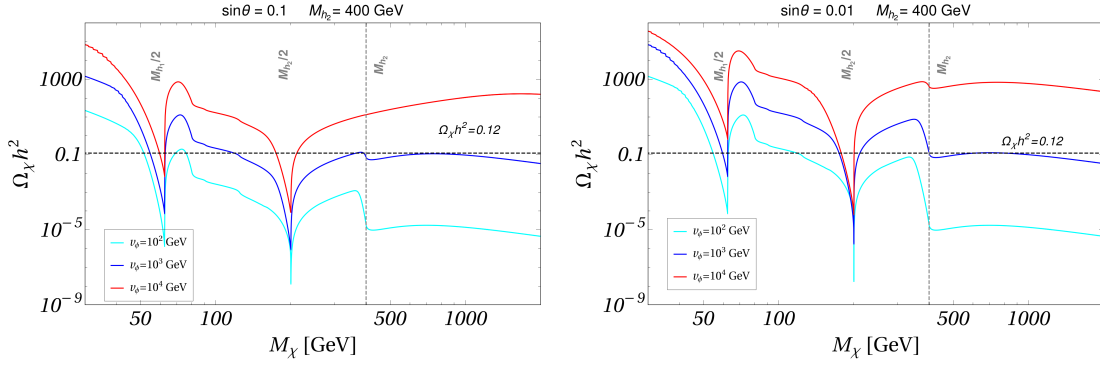


FIG. 7: Variation of relic density as a function of DM mass  $M_\chi$  for three values of  $v_\phi = 10^2, 10^3$  and  $10^4$  GeV corresponding to cyan, blue, and red lines respectively.  $M_{h_2} = 400$  GeV is fixed for both the panels, while the left (right) panel corresponds to  $\sin\theta = 0.1(0.01)$  respectively.

as follows.

- $M_\chi < M_{h_1}$  :  $\chi\chi \rightarrow \text{SM SM}$  with  $M_\chi > M_{\text{SM}}$  are the dominant number-changing processes which are mediated by both the CP-even physical states  $h_{1,2}$ . As discussed before, the relic density varies with both the  $\sin\theta$  and  $v_\phi$ .
- $M_{h_1} < M_\chi < M_{h_2}$  : New annihilation channels contribute to relic density depending on  $M_\chi$  as  $\chi\chi \rightarrow h_1 h_1$  with  $M_\chi > M_{h_1}$ ,  $\chi\chi \rightarrow t \bar{t}$  with  $M_\chi > M_t$  and  $\chi\chi \rightarrow h_1 h_2$  with  $M_\chi > (M_{h_1} + M_{h_2})/2$  ( $\sim 262.5$ ).
- $M_\chi > M_{h_2}$  : In addition to the aforementioned annihilation processes, the new process  $\chi\chi \rightarrow h_2 h_2$  also contributes to  $\langle\sigma v\rangle_{\text{eff}}$ . Consequently, there is a drop in relic density near  $M_\chi \sim M_{h_2}$ .

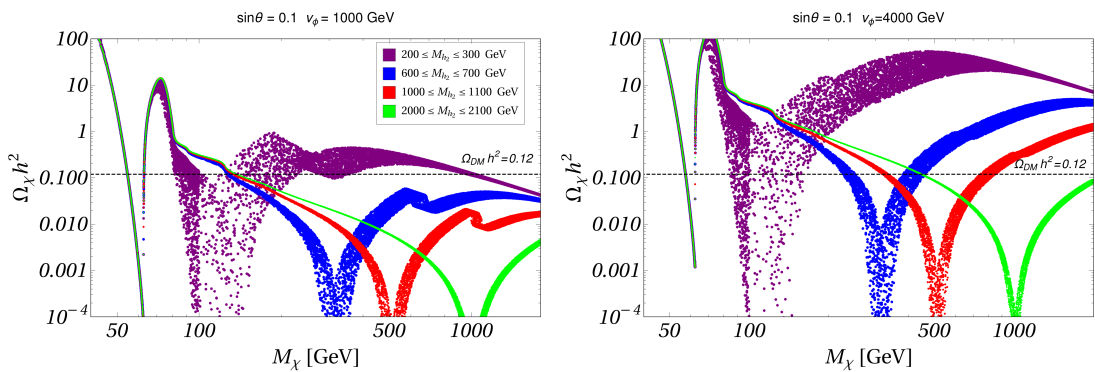


FIG. 8: Variation of relic density as a function of DM mass with different ranges of  $M_{h_2}$ .  $\sin\theta = 0.1$  is fixed for both the panels, while the left (right) panel corresponds to  $v_\phi = 1000$  (4000) GeV respectively.

Next, we show the variation of the DM relic density with  $M_\chi$  for four representative regions of  $M_{h_2}$  shown in both panels of Fig.8. The relic density is almost independent of  $M_{h_2}$  when DM mass is below  $M_W$ , as the coupling strengths between SM Higgs and light fermions are

suppressed. In contrast, when  $M_\chi > M_W$ ,  $M_{h_2}$  turns crucial and significantly affects the relic density as the DM annihilation into the gauge and scalar final states becomes available. In the presence of the new annihilation processes ( $\chi \chi \rightarrow h_1 h_2, h_2 h_2$ ) and the resonance-induced drop in relic density (discussed above), the  $M_{h_2}$  substantially influence the relic density of DM. This is due to the dependence of the quartic couplings ( $\lambda$ ) on  $M_{h_2}$  (see Eq.10). In Fig.8, we see that for fixed values of  $v_\phi$  and  $\sin\theta$ , the relic density decreases with the increase of  $M_{h_2}$  (for  $M_\chi > M_W$ ). This can be attributed to the fact that the portal coupling  $\lambda_{H\Phi}$  increases with the increase of  $M_{h_2}$  as illustrated in Eq.10. As discussed before, with the increase of  $v_\phi$ , the relic density of DM increases, shown in the right panel of Fig.8. Note that the relic density drops near  $M_\chi \sim M_{h_2}$  due to the opening of new annihilation process  $\chi \chi \rightarrow h_2 h_2$  and it becomes prominent for the lower value of  $v_\phi$  as  $\lambda_{H\Phi} \propto 1/v_\phi$ . That is the reason we have not observed any noticeable relic density drops near  $M_\chi \sim M_{h_2}$  for  $v_\phi = 4000$  GeV in the right panel of Fig.8.

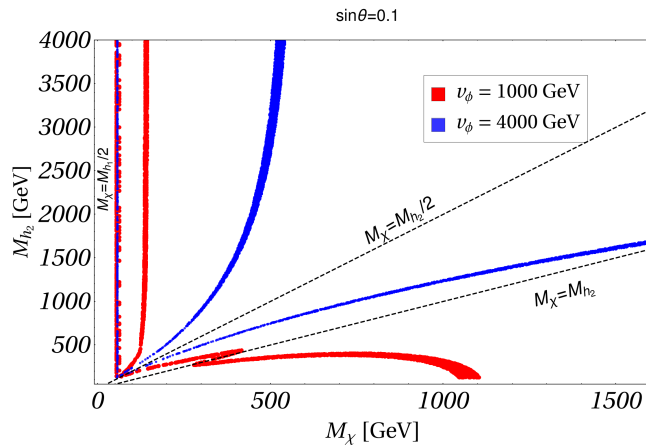


FIG. 9: The allowed parameter space for the relic density of DM ( $\Omega_\chi h^2 = 0.120 \pm 0.001$  [1]) in the plane of  $M_\chi$  vs  $M_{h_2}$  for fixed  $\sin\theta = 0.1$  and  $v_\phi = \{1000$  (Red),  $4000$  (Blue) $\}$  GeV. The dashed black lines correspond to  $M_\chi = M_{h_2}$  and  $M_\chi = M_{h_2}/2$  as mentioned on the representative lines of the figures.

In Fig.9, we show the relic allowed parameter space in  $M_\chi$  vs  $M_{h_2}$  plane for the same values of  $v_\phi$  and  $\sin\theta$ , considered in Fig.8. The vertical region around  $M_\chi \sim M_{h_1}/2$  satisfies the observed DM abundance, which is independent of  $M_{h_2}$  as mentioned earlier. For  $M_\chi > M_W$ , the observed relic density parameter space looks like a **V** shape in the plane of  $M_\chi - M_{h_2}$  for a fixed value of  $v_\phi$  (1000 GeV (red region) and 4000 GeV (blue region)). The region within each **V** shape corresponding to a fixed  $v_\phi$  represents the under-abundance ( $\Omega_\chi h^2 < \Omega_{\text{DM}} h^2$ ), while the region outside it represents over-abundance ( $\Omega_\chi h^2 > \Omega_{\text{DM}} h^2$ ). These regions can be

understood from both the figures in Fig.8. The diagonal dotted lines represent  $M_\chi = M_{h_2}$  and  $M_\chi = M_{h_2}/2$ , as depicted in the figure.

$v_\phi = 1000$  GeV (red region): First, we focus on the lower mass region of  $h_2$ , where  $M_{h_1} < M_{h_2} \lesssim 500$  GeV. The observed DM density is satisfied around  $M_\chi \sim M_{h_2}/2$  due to resonance. DM mass beyond the  $h_2$  pole, due to the opening of new annihilation processes  $\chi\chi \rightarrow h_2 h_2$ , DM relic density falls in the correct ballpark near DM mass  $M_\chi \sim M_{h_2}$ . At the same time with an increase in  $M_\chi$ , the coupling strengths  $\lambda_{h_i\chi\chi}$  and  $\lambda_{h_i h_j \chi\chi}$  also increase, resulting in a parameter space that satisfies the relic density for  $M_\chi \approx 500 - 1100$  GeV with  $M_{h_1} \lesssim M_{h_2} \lesssim 500$  GeV. In the heavier mass region of  $h_2$  with  $M_{h_2} \gtrsim 500$  GeV, the portal coupling  $\lambda_{H\Phi}$  gets enhanced, leading to under-abundance. However, there is a vertical region  $M_\chi \sim M_{h_1}$  that satisfies the observed dark matter density independently of  $M_{h_2}$ . In this mass region, the dark matter density decreases because of new number-changing processes and the enhanced cross-section near the  $h_2$  pole. These phenomena can be understood from the left panel of Fig.8, around the mass region  $M_\chi \sim M_{h_1}$ .

$v_\phi = 4000$  GeV (blue region): Similar feature can also be observed in this case. With an increase in  $v_\phi$ , the portal coupling is suppressed as  $\lambda_{H\Phi} \propto 1/v_\phi$ , resulting in a higher DM density. To satisfy relic density in this case, we rely on resonance enhancement in the  $\langle\sigma v\rangle_{\text{eff}}$  near the  $h_2$  pole. Therefore, it satisfies the observed DM abundance on both sides of  $M_\chi = M_{h_2}/2$  line with  $M_\chi > M_{h_1}/2$  and  $M_{h_1} < M_{h_2} \lesssim 2000$  GeV. Beyond  $M_{h_2} \gtrsim 2000$  GeV, the portal coupling  $\lambda_{\Phi H}$  is further enhanced with  $M_{h_2}$  as followed by Eq.10. This leads to an under-abundance for  $M_\chi \gtrsim 500$  GeV which can be understood from the right panel of Fig.8. Therefore there is a vertical region around  $M_\chi \sim 500$  GeV with  $M_{h_2} \gtrsim 2000$  GeV, regardless of  $M_{h_2}$ , which meets the observed relic density. In this region, the relic density falls due to resonance enhancement in the annihilation cross-section.

### A. Direct detection

We shall now move to the DM-nucleon scattering process relevant to direct detection (DD). In direct detection experiments, the flux of DM may scatter with the nuclei in the target crystals and the recoil rate of the target nucleus can be searched for as a signal of the DM. In this case, the spin-independent (SI)  $\chi - n$  scattering cross-section occurs via two CP even scalars ( $h_1$  and  $h_2$ ) exchange t-channel diagrams as shown in Fig.10. The corresponding spin-independent

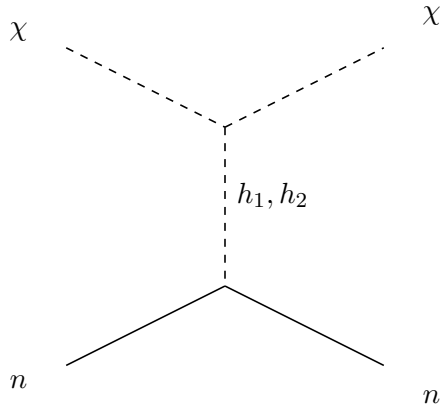


FIG. 10: Feynman diagrams for spin-independent DM-nucleon scattering process for DM ( $\chi$ ).

$\chi - n$  scattering cross-section with the fractional DM density  $f_\chi$  ( $\equiv \Omega_\chi/\Omega_{\text{DM}}$ ) is given by [53]

$$\begin{aligned} \sigma_{\text{DD}}^{\text{SI}} &= f_\chi \frac{1}{4\pi} \left( \frac{f_n \mu_n}{M_\chi} \right)^2 \left( \frac{m_n}{v} \right)^2 \left[ \frac{\lambda_{h_1\chi\chi} \cos \theta}{t - m_{h_1}^2} + \frac{\lambda_{h_2\chi\chi} \sin \theta}{t - m_{h_2}^2} \right]^2 \\ &\stackrel{t \rightarrow 0}{=} f_\chi \frac{1}{4\pi} \left( \frac{f_n \mu_n}{M_\chi} \right)^2 \left( \frac{m_n}{v} \right)^2 \left[ \frac{\lambda_{h_1\chi\chi} \cos \theta}{m_{h_1}^2} + \frac{\lambda_{h_2\chi\chi} \sin \theta}{m_{h_2}^2} \right]^2, \end{aligned} \quad (39)$$

where

$$\begin{aligned} \lambda_{h_1\chi\chi} &= -\lambda_{H\Phi} v \cos \theta + 2\lambda_\Phi v_\phi \sin \theta - \frac{3\mu_3 \sin \theta}{\sqrt{2}} \\ \text{and } \lambda_{h_2\chi\chi} &= -\lambda_{H\Phi} v \sin \theta - 2\lambda_\Phi v_\phi \cos \theta + \frac{3\mu_3 \cos \theta}{\sqrt{2}}. \end{aligned}$$

Here  $\mu_n = \frac{m_n M_\chi}{m_n + M_\chi}$  is the reduced mass of DM-nucleon system with  $m_n = 0.946$  GeV (neutron mass) and  $f_n = 0.28$  is the nucleon form factor [54]. For small  $\sin \theta$  limit the cross-section turns out to be  $\sigma_{\text{DD}}^{\text{SI}} \propto \frac{\lambda_{H\Phi}^2}{M_\chi^2}$  where the expression of  $\lambda_{H\Phi}$  is given in Eq.10. Non-observation of DM at direct search experiments such as XENON-1T [18], PANDAX-4T [19] and most recent LZ 2022 [20] put stringent constraints on the  $M_\chi - \sigma_{\text{DD}}^{\text{SI}}$  plane which can be translated in terms of the model parameters.

We plot the relic density allowed parameter space ( $f_\chi = 1$  i.e. 100% of the observed relic density) in  $M_\chi$  vs  $\sigma_{\text{DD}}^{\text{SI}}$  plane in Fig.11 (a) to compare with the current upper bounds from XENON-1T[18], PANDAX 4T[19], and LZ 2022 [20]. The red region corresponds to  $v_\phi = 1000$  GeV, and the blue region corresponds to  $v_\phi = 4000$  GeV, both with  $\sin \theta = 0.1$ . The increase in  $v_\phi$  leads to a decrease in the DM-nucleon scattering cross-section due to the suppression of the portal coupling  $\lambda_{H\Phi}$  with higher  $v_\phi$  which is depicted in Fig.11 (a). Therefore, for  $v_\phi = 4000$  GeV the SI DD cross-section becomes smaller compared to  $v_\phi = 1000$  GeV and remains unconstrained by DD experiments. The current LZ 2022 [20] data excludes our parameter space in the intermediate-mass region  $M_\chi \sim \{300 - 1000\}$  GeV with  $M_{h_2} \lesssim 500$  GeV for  $v_\phi = 1000$

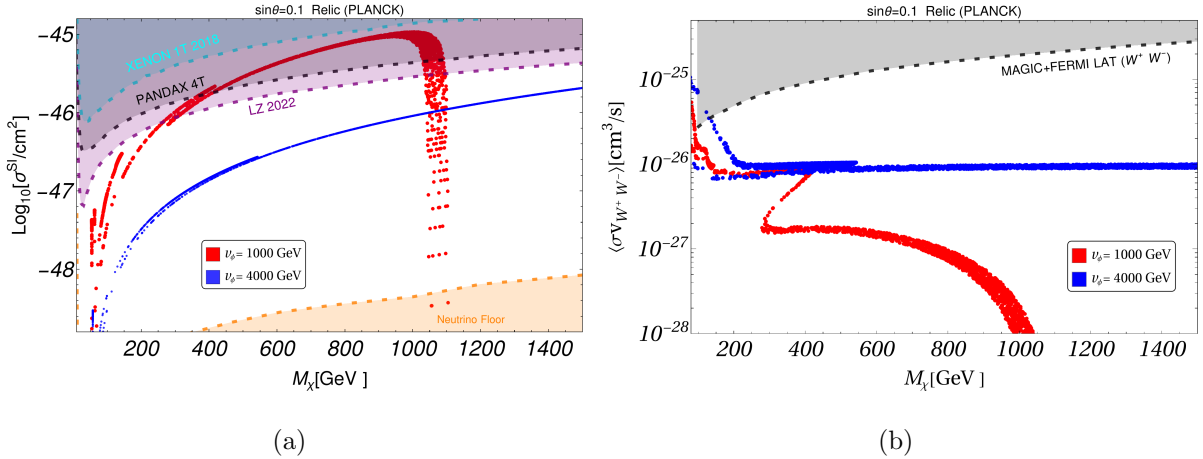


FIG. 11: (a) Relic density allowed parameter space is plotted in the plane of DM mass versus SI DM-nucleon cross-section for  $v_\phi = 1000$  GeV (red region) and  $v_\phi = 4000$  GeV (blue region) while keeping  $\sin\theta = 0.1$ . We compare the parameter space with the experimental upper bounds from XENON-1T[18], PANDAX 4T[19], LZ 2022 [20] in the same plane. The orange shaded region represents the neutrino floor. (b) The thermally averaged cross-section of the  $\chi\chi \rightarrow W^+W^-$  process for the parameter space allowed by observed DM density (PLANCK) is plotted as a function of  $M_\chi$ . The combined exclusion bound from indirect search experiments by Fermi-LAT [21] and MAGIC [22] is shown in the gray region for the same DM annihilation channel. Note that for both the plots,  $\chi$  represents 100% ( $f_\chi = 1$ ) of the observed DM density.

GeV. There is a drop in  $\sigma_{\text{DD}}^{\text{SI}}$  near  $M_\chi \sim 1000$  GeV with  $v_\phi = 1000$  GeV. This phenomenon occurs because the observed DM relic density in this region demands a lower  $M_{h_2}$ , as discussed earlier. As a result, the cross-section decreases since  $\lambda_{H\Phi}$  diminishes with  $M_{h_2}$ .

## B. Indirect detection

DM can also be detected at various indirect search experiments, including space-based observatories like the Fermi-LAT [21] and ground-based counterparts like MAGIC [22] telescopes. These telescopes detect gamma rays produced via DM annihilation or decay in the local Universe. In our discussion, the gamma-ray flux can be produced when DM  $\chi$  annihilates into SM-charged particle pairs ( $\psi^+\psi^-$ ), followed by their subsequent decay. The total gamma-ray flux for a given mode  $\chi\chi \rightarrow \psi^+\psi^-$  ( $\psi = \{\mu, \tau, b, W\}$ ) in a specific energy range is given by [22]

$$\Phi_{\psi^+\psi^-}^\gamma = \frac{1}{4\pi} \frac{\langle\sigma v\rangle_{\chi\chi \rightarrow \psi^+\psi^-}}{2M_\chi^2} \int_{E_{\text{min}}}^{E_{\text{max}}} \frac{dN_\gamma}{dE_\gamma} dE_\gamma \int dx \rho_\chi^2(r(b, l, x)) \quad (40)$$

The notation follows standard conventions as ref. [22]. The indirect search experiments like Fermi-LAT and MAGIC [21, 22] collectively put an upper bound  $\langle\sigma v\rangle_{\chi\chi \rightarrow \psi^+\psi^-}$  from the non-

observation of gamma-ray flux produced from DM. It is evident from the above Eqn.40, to compare the experimental bounds with the theoretical  $\langle\sigma v\rangle_{\chi\chi\rightarrow\psi^+\psi^-}$ , one must scale the cross-section by the fractional DM abundance as:  $\langle\sigma v\rangle_{\chi\chi\rightarrow\psi^+\psi^-}^{\text{ID}} = f_\chi^2\langle\sigma v\rangle_{\chi\chi\rightarrow\psi^+\psi^-}$  with  $f_\chi = \Omega_\chi/\Omega_{\text{DM}} (\leq 1)$ .

The most stringent constraint is found to come from the DM annihilation mode  $\chi\chi \rightarrow W^+W^-$  compared to other modes, due to the gauge coupling. In Fig.11 (b), we show  $\langle\sigma v_{W^+W^-}\rangle$  as a function of  $M_\chi$  for all relic satisfied points with  $f_\chi = 1$  ( $\chi$  contributes 100% of the observed relic density), and compare it with the combined Fermi-LAT and MAGIC exclusion bound [21, 22], shown in the gray region. Similar to the DD cross-section, the  $\langle\sigma v_{W^+W^-}\rangle$  decreases with an increase in  $v_\phi$  (shown in red for 1000 GeV and in blue for 4000 GeV) and a decrease in  $M_{h_2}$ , which is influenced by the coupling  $\lambda_{H\Phi}$  (see Eq.10). From the plot, it turns out that apart from lower  $M_\chi$ , most of the parameter space lies below the combined Fermi-LAT and MAGIC exclusion bound. Note that the other DM annihilation modes  $\psi^+\psi^- : \{b\bar{b}, \tau^+\tau^-, \mu^+\mu^-\}$  are well below the upper bound set by indirect searches, due to the relatively suppressed SM Yukawa coupling with the fermions.

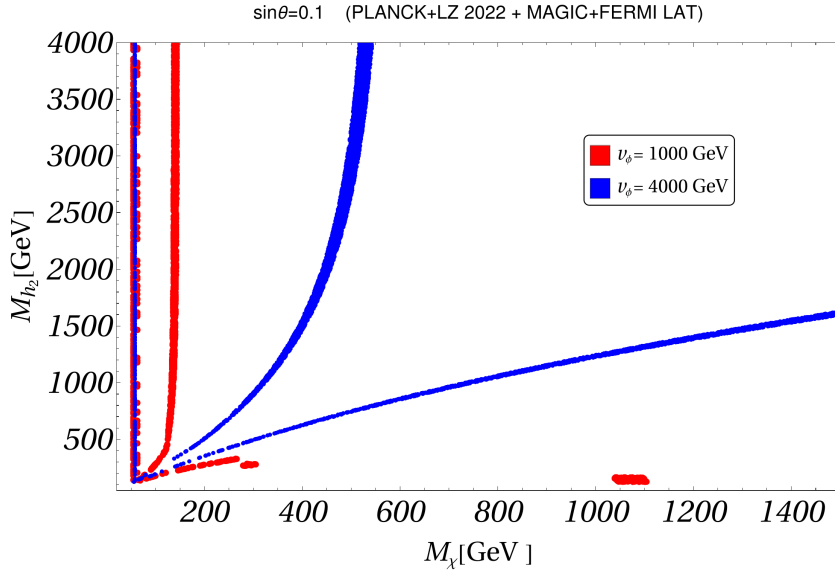


FIG. 12: Relic (PLANCK) + DD (LZ 2022) + ID (Fermi LAT + MAGIC) allowed parameter space is shown in the plane of  $M_\chi$  and  $M_{h_2}$  for the same parameters. Here DM ( $\chi$ ) contributes 100% of the observed relic density ( $f_\chi = 1$ ).

Finally in Fig.12, we show the parameter space in  $M_\chi - M_{h_2}$  plane which collectively satisfies Relic (PLANCK [1]) + DD (LZ 2022 [20]) + ID (Fermi LAT + MAGIC [21, 22]) constraints. The red and blue regions correspond to the  $v_\phi = 1000$  GeV and  $v_\phi = 4000$  GeV respectively with  $\sin\theta = 0.1$ . Note that the intermediate DM mass region  $M_\chi \sim \{300 - 1000\}$  GeV for  $v_\phi = 1000$  GeV is excluded from the upper bound on DM-nucleon cross-section by LZ 2022 [20].

## V. PHASE TRANSITION

We now discuss the possibility of a strong first-order phase transition in the parameter space relevant to both Leptogenesis and Dark Matter phenomenology. Our main objective for studying FOPT is that they can give rise to stochastic GWs which can be detected by experiments in the future. The physics comprising of low-scale Leptogenesis and Dark Matter phenomenology leave their imprints on the GW spectrum which can be detected in GW detectors. For the study of phase transition in this model, we consider the effective potential of the model at finite temperatures.

The Coleman Weinberg effective potential (or the quantum corrections to the tree level potential) at one loop level in the  $\overline{\text{MS}}$  renormalisation scheme at zero temperature is given by [55]

$$V_{\text{cw}}(h_i) = \sum_{j=W^\pm, Z, h_1, h_2, \chi, t} (-1)^{S_j} \frac{n_j m_j^4(h_i)}{64\pi^2} \left[ \log \frac{m_j^2(h_i)}{4\pi\mu^2} - C_j \right] \quad (41)$$

where in the above equation  $h_i$  are the scalar fields in physical basis with  $\{i = 1, 2\}$ ,  $m_j$  are the masses of the  $j^{\text{th}}$  particle and  $n_j$  are the degrees of freedom of the  $j^{\text{th}}$  particle.  $S_j$  has the value 0 for bosons and 1 for fermions.  $\mu$  is the renormalisation energy scale which is taken to be  $m_t$ .  $C_j$  are the constants which have the value  $\frac{3}{2}$  for scalars and fermions and  $\frac{5}{6}$  for gauge bosons. Considering thermal effects, the temperature-dependent part of the effective potential at one loop level can be expressed as [56]

$$V_T(h_i, T) = \frac{T^4}{2\pi^2} \left[ \sum_B n_B J_B(m_B^2(h_i)/T^2) + \sum_F n_F J_F(m_F^2(h_i)/T^2) \right]. \quad (42)$$

The  $n_{B/F}$  are the degrees of freedom of bosons/fermions respectively and the  $J_{B/F}$  are Bosonic and Fermionic functions which are represented as

$$J_{B/F}(x^2) = \int_0^\infty y^2 \log[1 \mp e^{-\sqrt{x^2+y^2}}] dy. \quad (43)$$

At the high-temperature limit, one can expand the Bosonic and Fermionic integrals in powers of  $x \equiv m/T$  as [57]:

$$\begin{aligned} J_B(x^2) |_{x \ll 1} &\simeq -\frac{\pi^4}{45} + \frac{\pi^2}{12}x^2 - \frac{\pi}{6}x^3 + \mathcal{O}(x^4), \\ J_F(x^2) |_{x \ll 1} &\simeq \frac{7\pi^4}{360} - \frac{\pi^2}{24}x^2 + \mathcal{O}(x^4). \end{aligned} \quad (44)$$

Therefore, at the high-temperature limit, thermal corrected one-loop effective potential can be written using Eq.44 as:

$$V_T(h_i, T) = \frac{T^2}{24} \sum_j n_j m_j^2(h_i). \quad (45)$$

At high temperatures, the perturbative expansion of the effective potential may not remain valid. The divergent terms (infrared divergence) that arise from the Matsubara modes while considering finite temperature effects require resummation by replacing the field-dependent masses with their respective thermal masses at one loop propagator. So, in addition to the one-loop thermal corrections, we can have contributions from ring diagrams and thus we have to consider Daisy resummation to the effective potential. To expand the effective potential, we use the Parwani method [58]. The potential due to such ring diagrams can be written as [59],

$$V_{\text{ring}}(h_i, T) = - \sum_j \frac{n_j T}{12\pi} \left( [m_j^2(h_i) + \Pi_j(T)]^{\frac{3}{2}} - m_j^3(h_i) \right) \quad (46)$$

The quantities  $m_j^2(h_i) + \Pi_j(T)$  are called the thermal masses. The quantities  $\Pi_j$  are called the Daisy Coefficients which are obtained from the coefficients of  $T^2$  in the expression of finite temperature correction to the effective potential in the high temperature limit.

The double derivative of Eq.45 with respect to the CP-even scalar fields will give the Daisy coefficient matrix  $\Pi$  for the CP-even scalar fields and is given by

$$\begin{bmatrix} \frac{\lambda_H}{4} + \frac{\lambda_{H\Phi}}{24} + \frac{3g^2}{16} + \frac{g'^2}{16} + \frac{y^2}{4} & 0 \\ 0 & \frac{\lambda_\Phi}{4} + \frac{\lambda_{H\Phi}}{24} \end{bmatrix} T^2. \quad (47)$$

While taking into account the Coleman Weinberg at zero temperature corrections, generally the tree level vevs and the masses get changed. To avoid that, we have to add zero temperature counter term  $\delta V_{\text{ct}}(h_i)$  to the effective potential which is given by,

$$\begin{aligned} \delta V_{\text{ct}}(h_i) = & -\delta\mu_H^2(H^\dagger H) + \delta\lambda_H(H^\dagger H)^2 - \delta\mu_\Phi^2(\Phi^\dagger\Phi) + \delta\lambda_\Phi(\Phi^\dagger\Phi)^2 \\ & + \delta\lambda_{H\Phi}(\Phi^\dagger\Phi)(H^\dagger H) + \frac{\delta\mu_3}{2}(\Phi^3 + \Phi^{\dagger 3}). \end{aligned} \quad (48)$$

To find out the expressions of the counter terms corresponding to each parameter, we use the following conditions,

$$\begin{aligned} \partial_{h_a}(\delta V_{\text{ct}} + \Delta V) &= 0, \\ \partial_{h_a}\partial_{h_b}(\delta V_{\text{ct}} + \Delta V) &= 0, \end{aligned} \quad (49)$$

where the partial derivatives are taken with respect to  $h$  and  $\phi$  fields expressed as  $h_{a(b)}$ . The derivatives are evaluated at  $h = v$  and  $\phi = v_\phi$ . The  $\Delta V$  is the effective potential at zero temperature excluding the tree-level part of the potential. The expressions of the counter term containing  $\delta V_{\text{ct}}$  corresponding to each parameter in the tree level potential are given in VIII C. The final expression of the total effective potential is given by

$$V(h_i, T) = V_0(h_i) + V_{\text{cw}}(h_i) + V_T(h_i, T) + V_{\text{ring}}(h_i, T) + \delta V_{\text{ct}}(h_i) \quad (50)$$

where  $V_0(h_i)$  is the tree level potential given by Eq.2 expressed in the physical basis.<sup>3</sup>

In general, phase transition involves an important quantity that characterizes the transition between two phases and is called the critical temperature. In the context of a FOPT, the critical temperature  $T_c$  is determined by equating the potential values at the two vev's, corresponding to the high vev and the low vev, respectively, which is given by [60]

$$V(h_i^{\text{High}}, T_c) = V(h_i^{\text{Low}}, T_c). \quad (51)$$

Strong FOPT (SFOPT) will generate Gravitational waves with high amplitudes that can have a significant overlap with the sensitivity regions of upcoming GW detectors. The condition of strong first-order phase transition is given by  $\zeta_c \geq 1$  where the quantity  $\zeta_c$  is called the order parameter and is expressed as

$$\zeta_c = \frac{\Delta h_i}{T_c}, \quad (52)$$

with  $\Delta h_i$  is the difference between high and low vevs of the SM/BSM scalar field.

It is important to note that the total effective potential given in Eq.50 depends on the gauge explicitly. Thus the important ingredients that are required for the study of phase transition, namely the order parameter  $\zeta_c$ , and also the extremas of the effective potential are gauge dependent[56, 60–63]. In our case, all the finite temperature calculations are done in Landau gauge ( $\xi = 0$ ).<sup>4</sup>

We generate the results of the phase structures of the scalar fields using the publicly available CosmoTransition package [66]. We present four Benchmark Points representing SFOPT in Table III contained in Sec.VI. In our analysis, we obtain two main phase transition patterns which we characterize as Type A and Type B phase transitions.

- **Type A:** single-step, first-order phase transition.
- **Type B:** two-step, the first step is first-order while the second step is second-order.

BP 1 and BP 2 fall in the Type A category while BP 3 and BP 4 fall in the Type B category. We represented the phase structure of the fields as a function of the temperature of BP 1 and BP 3 as an example of Type A and Type B phase transition respectively in Fig.16 of Sec.VI. Further detailed discussions regarding the phase structure of the BPs are provided in Sec.VI.

---

<sup>3</sup> In our numerical analysis, we employ the full integrals  $J_{B/F}$  as defined in Eq.43, rather than the approximate expressions  $J_{B/F}$  given in Eq.44 that are valid at high temperatures.

<sup>4</sup> As the effective potential calculations depend on the gauge choice explicitly, a gauge-independent detailed analysis is beyond the scope of this paper. Further details can be found in [64, 65].

## A. Gravitational Wave Spectrum

Cosmological phase transitions in the early Universe can give rise to stochastic Gravitational waves. The generation of such waves necessitates a strong first-order phase transition. These GWs originate from the release of energy of the colliding bubbles of the true vacuum as they propagate throughout the entire plasma. Such bubble formation can only take place in first-order phase transitions. A FOPT can be analyzed by two main temperatures which are the critical temperature  $T_c$  and the nucleation temperature  $T_n$ . The FOPT proceeds via bubble nucleation at  $T_n$  which is in general, slightly below  $T_c$ . During nucleation, the tunneling probability per unit volume at a finite temperature  $T$  from the false vacuum to the true vacuum is given by [67]

$$\Gamma(T) = T^4 \left( \frac{S_3}{2\pi T} \right)^{\frac{3}{2}} e^{-\frac{S_3}{T}}, \quad (53)$$

where  $S_3$  represents the 3 dimensional Euclidean Action and is given by [68]

$$S_3 = 4\pi \int r^2 dr \left[ \frac{1}{2} \left( \frac{dh_i}{dr} \right)^2 + V_{eff}(h_i, T) \right] \quad (54)$$

The differential equation satisfied by the scalar fields  $h_i$  where  $i = 1, 2$  is given by [68–70]

$$\frac{d^2 h_i}{dr^2} + \frac{2}{r} \frac{dh_i}{dr} = \frac{dV_{eff}(h_i, T)}{dh_i} \quad (55)$$

with the boundary conditions  $h_i = 0$  as  $r \rightarrow \infty$  and  $\frac{dh_i}{dr} = 0$  at  $r = 0$ .

There are three main sources of the generation of the stochastic Gravitational waves which are:

- The Bubbles of the true vacuum collide with each other and the energy of collision is propagated in the form of Gravitational Waves.
- Sound waves are generated in the plasma when the bubbles are propagating through it.
- Magnetohydrodynamic turbulence forming in the plasma after the collision of the bubbles.

In general, these three sources co-exist and the total Gravitational Wave energy spectrum can be expressed as [71, 72]

$$\Omega_{\text{GW}} h^2 \simeq \Omega_{\text{col}} h^2 + \Omega_{\text{sw}} h^2 + \Omega_{\text{turb}} h^2. \quad (56)$$

The GW spectrum depends upon four important parameters. They are:

- (i)  $\alpha$ : A quantity that is proportional to the latent heat corresponding to the phase transition and indicates the strength of the phase transition.
- (ii)  $\frac{\beta}{H_n}$ : A quantity that is inversely proportional to the time taken for the phase transition to

complete.

(iii)  $T_n$ : The Nucleation temperature.

(iv)  $v_w$ : Velocity of the Bubble Wall.

Among these parameters,  $\alpha$  signifies the strength of the phase transition and is expressed as [73]

$$\alpha = \frac{\epsilon(T_n)}{\rho_R(T_n)}, \quad (57)$$

where  $\epsilon$  is expressed as [74]

$$\epsilon(T_n) = \Delta V_{eff} - T \left. \frac{d\Delta V_{eff}}{dT} \right|_{T=T_n}. \quad (58)$$

The  $\Delta V_{eff}$  is the difference between the effective potentials at false and true vacuum and  $\rho_R(T_n)$  is the energy density of radiation given by,

$$\rho_R(T_n) = \frac{\pi^2 g_* T_n^4}{30}, \quad (59)$$

with  $g_*$  representing the relativistic degrees of freedom at  $T_n$ . The parameter  $\frac{\beta}{H_n}$  denotes the ratio of the inverse time duration of the phase transition to the Hubble parameter value at  $T_n$  and can be expressed as [75]

$$\frac{\beta}{H_n} = T_n \left. \frac{d(S_3/T)}{dT} \right|_{T=T_n}. \quad (60)$$

The part of the GW spectrum resulting from bubble collisions, red-shifted to today, can be expressed as [76]

$$\Omega_{col} h^2 = 1.67 \times 10^{-5} \left( \frac{\beta}{H_n} \right)^{-2} \left( \frac{\kappa_{col} \alpha}{1 + \alpha} \right)^2 \left( \frac{100}{g_*} \right)^{\frac{1}{3}} \left( \frac{0.11 v^3}{0.42 + v^2} \right) \left( \frac{3.8 \left( \frac{f}{f_{col}} \right)^{2.8}}{1 + 2.8 \left( \frac{f}{f_{col}} \right)^{3.8}} \right), \quad (61)$$

where we have the peak frequency  $f_{col}$  red-shifted to today as [76]

$$f_{col} = 1.65 \times 10^{-5} \left( \frac{0.62}{1.8 - 0.1 v_w + v_w^2} \right) \left( \frac{\beta}{H_n} \right) \left( \frac{T_n}{100} \right) \left( \frac{g_*}{100} \right)^{1/6}. \quad (62)$$

The efficiency factor for bubble collision is expressed as [77],

$$\kappa_{col} = \frac{0.715\alpha + \frac{4}{27} \sqrt{\frac{3\alpha}{2}}}{0.715\alpha + 1}. \quad (63)$$

As the bubble of true vacuum propagates through the plasma, they produce sound waves. The part of the GW spectrum resulting from these sound waves, red-shifted to today, can be expressed as [78–81]

$$\Omega_{sw} h^2 = 2.65 \times 10^{-6} \Gamma_{sw} \left( \frac{\beta}{H_n} \right)^{-1} v_w \left( \frac{\kappa_{sw} \alpha}{1 + \alpha} \right)^2 \left( \frac{g_*}{100} \right)^{\frac{1}{3}} \left( \frac{f}{f_{sw}} \right)^3 \left( \frac{4}{7} + \frac{3}{7} \left( \frac{f}{f_{sw}} \right)^2 \right)^{-\frac{7}{2}}, \quad (64)$$

where  $\Gamma_{\text{sw}}$  is the suppression factor arising from the finite lifetime of the sound waves generated with  $\tau_{\text{sw}}$  being the lifetime of the sound waves and  $U$  is the root mean square velocity of the sound waves. These three quantities are expressed by, [80]

$$\Gamma_{\text{sw}} = \left(1 - \frac{1}{\sqrt{1 + 2\tau_{\text{sw}}H_n}}\right), \quad \tau_{\text{sw}} = \frac{(8\pi)^{\frac{1}{3}}}{\beta U}, \quad U = \sqrt{\frac{3}{4}\alpha\kappa_{\text{sw}}}. \quad (65)$$

The peak frequency of the sound waves redshifted to today is expressed as, [80]

$$f_{\text{sw}} = 1.9 \times 10^{-5} \left(\frac{1}{v_w}\right) \left(\frac{\beta}{H_n}\right) \left(\frac{T_n}{100}\right) \left(\frac{g_*}{100}\right)^{1/6}. \quad (66)$$

The efficiency factor corresponding to the contribution of the sound waves is given by [77],

$$\kappa_{\text{sw}} = \frac{\alpha}{\alpha + 0.083\sqrt{\alpha} + 0.73}. \quad (67)$$

The part of the GW spectrum resulting from magnetohydrodynamic turbulence generated within the ionized plasma, red-shifted to today, can be expressed as [82]

$$\Omega_{\text{turb}}h^2 = 3.35 \times 10^{-4} \left(\frac{\beta}{H_n}\right)^{-1} v_w \left(\frac{\kappa_{\text{turb}}\alpha}{1 + \alpha}\right)^{\frac{3}{2}} \left(\frac{100}{g_*}\right)^{\frac{1}{3}} \left(\frac{\left(\frac{f}{f_{\text{turb}}}\right)^3}{\left(1 + \left(\frac{f}{f_{\text{turb}}}\right)^{\frac{11}{3}}\right) \left(1 + \frac{8\pi f}{h_*}\right)}\right) \quad (68)$$

where  $h_*$  is the inverse Hubble time during the production of Gravitational Waves,

$$h_* = 16.5 \times \left(\frac{T_n}{100}\right) \left(\frac{g_*}{100}\right)^{1/6}. \quad (69)$$

The peak frequency due to turbulence generated in the ionized plasma due to the magnetic fields in the plasma, redshifted to today can be expressed as,[82]

$$f_{\text{turb}} = 2.7 \times 10^{-5} \left(\frac{1}{v_w}\right) \left(\frac{\beta}{H_n}\right) \left(\frac{T_n}{100}\right) \left(\frac{g_*}{100}\right)^{1/6}. \quad (70)$$

The  $\kappa_{\text{turb}}$  represents the efficiency factor corresponding to the contribution of MHD turbulence and is generally given in terms of a small fraction of  $\kappa_{\text{sw}}$ . We consider  $\kappa_{\text{turb}} = 0.1\kappa_{\text{sw}}$  as suggested by simulations [77].

The above expressions of the efficiency factors  $\kappa_{\text{col}}$  and  $\kappa_{\text{sw}}$  are valid for relativistic bubble wall velocity (in the limit  $v_w \rightarrow 1$ ) which we consider in our work.

To determine the detectability of any signal from the background, the most commonly used quantity is the Signal-to-noise ratio (SNR) which is defined below [72]

$$\text{SNR} \equiv \sqrt{\tilde{T} \int_{f_{\text{min}}}^{f_{\text{max}}} \left[\frac{h^2 \Omega_{\text{GW}}(f)}{h^2 \Omega_{\text{Sens}}(f)}\right]^2 df}. \quad (71)$$

We have considered  $\tilde{T}$  to be of 5 years duration for all the relevant detectors. The  $h^2 \Omega_{\text{Sens}}(f)$  corresponds to the experimental sensitivity of a given experimental configuration to cosmological sources obtained from the power spectral density (PSD)  $S_h(f)$  [83].

## VI. RESULTS AND ANALYSIS

In this section, we first identify a common parameter space that can explain both observed BAU and the abundance of Dark Matter. Next, we examine the parameter space for Gravitational waves generated during the first-order phase transition. We concentrate on the scenario where the scalar mass  $M_\phi$  is heavier than the SM Higgs boson mass. Finally, we present our findings in terms of the mass eigenstate  $M_{h_2}$  as defined in Eq.12 instead of using  $M_\phi$  directly. Note that, as  $\sin\theta \rightarrow 0$ ,  $M_\phi \simeq M_{h_2}$ . As discussed earlier, at the Leptogenesis scale the  $\xi$  is a function of  $\lambda_{H\phi}$  and  $v_\phi$ . Following scalar mixing, the coupling  $\lambda_{H\Phi}$  can be rewritten in terms of low energy parameters  $v_\phi$ ,  $\sin\theta$  and  $M_{h_2}$  as shown in Eq.10. We fix our choice for the  $\sin\theta = \{0.3, 0.1, 0.01\}$  and for the  $v_\phi = \{1000, 4000\}$  GeV. Fig.14 shows the common and compatible parameter space for the observed baryon asymmetry of the Universe (left column) and the allowed abundance of the DM (right column) in the plane of  $M_{h_2} - \lambda_{H\Phi}$ .

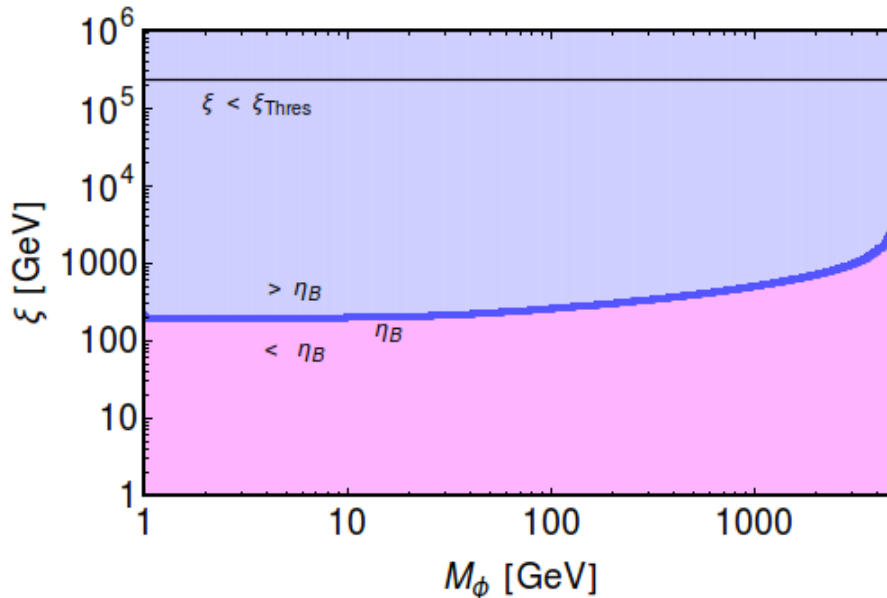


FIG. 13: The allowed parameter space of the observed baryon asymmetry of the Universe in the plane of  $M_\phi$  and  $\xi$ . The Blue and Pink color region represents the over- and under-abundant baryon asymmetry. Here  $M_{N_2} = 5.5 \times 10^4$  GeV and  $M_{N_1} = 5 \times 10^4$  GeV corresponding to  $\delta M = 0.1$  and  $\alpha_{ij} = 8 \times 10^{-3}$ .

In Fig.14, we consider the mass of right-handed neutrinos  $M_{N_2} = 5.5 \times 10^4$  GeV and  $M_{N_1} = 5 \times 10^4$  GeV corresponding to  $\delta M = 0.1$  and  $\alpha_{ij} = 8 \times 10^{-3}$ . For an illustration, we consider the same parameter choice and present the BAU allowed parameter space in Fig.13 at the Leptogenesis scale (before EWSB) in the plane of  $M_\phi$  and  $\xi$ . The blue line corresponds to the observed baryon asymmetry of the Universe. The light-blue and pink regions correspond to over and under-abundant baryon asymmetry respectively. After EWSB, the  $M_\phi$  and  $\xi$  can

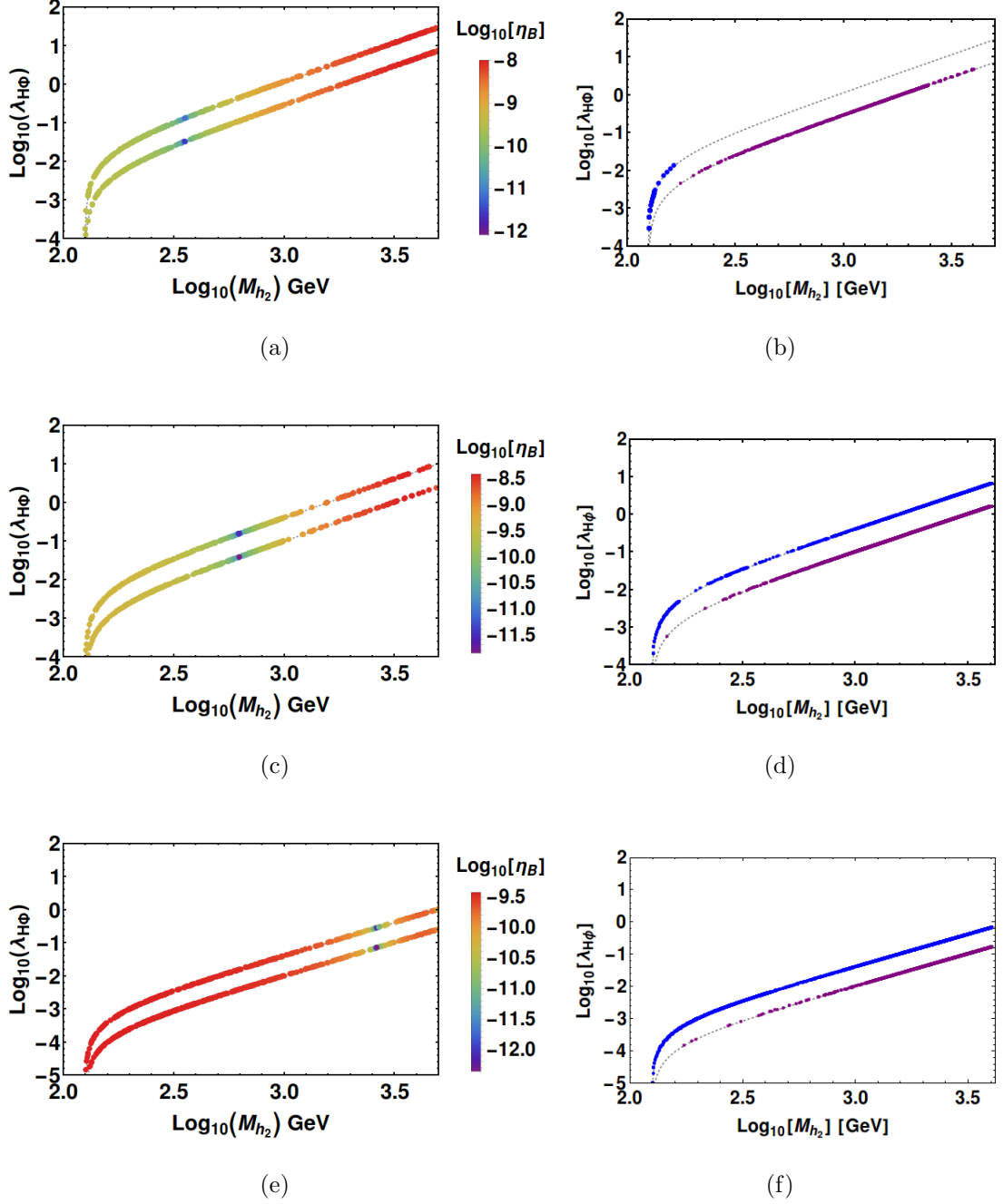


FIG. 14: Figure shows the allowed parameter space for both the baryon asymmetry of the Universe (left column) and Dark Matter abundance (right column) in the plane of  $M_{h_2}$  -  $\lambda_{H\Phi}$ .  $M_{N_2} = 5.5 \times 10^4$  GeV,  $M_{N_1} = 5 \times 10^4$  GeV. The top, middle, and bottom row panels correspond to  $\sin \theta = 0.3, 0.1, \text{ and } 0.01$ , respectively. Each plot's top and bottom lines correspond to  $v_\phi = 1000, 4000$  GeV respectively. The Grey dashed line represents the Eq.10 for  $\lambda_{H\Phi}$ .

be re-expressed in the plane of  $M_{h_2}$  and  $\lambda_{H\Phi}$ , Fig.14, for a fixed set of values of  $\sin \theta$  and  $v_\phi$ . The top, middle, and bottom panels correspond to  $\sin \theta = 0.3, 0.1, 0.01$  respectively. In each plot top and bottom lines correspond to  $v_\phi = 1000$  and  $4000$  GeV respectively. Unlike the  $M_\phi$ , the baryon asymmetry increases gradually with the  $M_{h_2}$  increase, since  $M_{h_2}$  is proportional to

$\lambda_{H\Phi}$ . Hence with the increase in  $\lambda_{H\Phi}$  the baryon asymmetry increases. In Fig.14, the decline in baryon asymmetry (blue points), arises due to the competitive interplay between  $M_{h_2}$  and the corresponding Higgs portal coupling  $\lambda_{H\Phi}$ . As the  $M_{h_2}$  increases, the baryon asymmetry slowly diminishes, similar to the pattern shown in Fig.3. However, a rise in  $\lambda_{H\Phi}$  leads to a greater increase in the baryon asymmetry beyond a certain point relative to the effect of increasing  $M_{h_2}$ . Before this  $\lambda_{H\Phi}$  contribution to the baryon asymmetry dominates once again, a drop occurs due to the increase in  $M_{h_2}$ . We show the drop in baryon asymmetry of Fig.14 correspond to the  $\sin \theta = 0.1$  and for  $v_\phi = 1000$  GeV, as an example, in Fig.15. The yellow region is the maximum baryon asymmetry achievable for our parameter choice. The horizontal Grey dashed line represents the observed BAU. The observed baryon asymmetry can be seen in Table.II: i) for  $M_{h_2} \sim 600$  GeV and  $\lambda_{H\Phi} \sim 0.4(1000 \text{ GeV}), 0.1(4000 \text{ GeV})$  for fixed  $\sin \theta = 0.3$ . ii) for  $M_{h_2} \sim 1130$  GeV and  $\lambda_{H\Phi} \sim 0.5(1000 \text{ GeV}), 0.13(4000 \text{ GeV})$  for fixed  $\sin \theta = 0.1$ . For  $\sin \theta = 0.01$  the baryon asymmetry is seen under-abundant.

The Blue and Purple color points that appear in the right column of Fig.14 correspond to the Relic+DD+ID allowed parameter space of Dark Matter correspond to  $v_\phi = 1000$  and  $4000$  GeV respectively. We observe that the parameter space corresponding to Dark Matter phenomenology is consistent with the observed baryon asymmetry of the Universe for  $\sin \theta = 0.3, v_\phi = 4000$  GeV (top panel), and for  $\sin \theta = 0.1, v_\phi = 1000$  and  $4000$  GeV (middle panel). Whereas, the baryon asymmetry is under-abundant for  $\sin \theta = 0.01$  (bottom panel). We see that the observed BAU can be satisfied for the large value of  $\sin \theta = 0.3$  with two choices of  $v_\phi$ , but the DM Relic+DD+ID is allowed only with the large value of  $v_\phi = 4000$  GeV. The Relic+DD+ID may be permitted for small  $\sin \theta = 0.01$  with two  $v_\phi$  choices but the baryon asymmetry is seen under-abundant. We observe that, for the parameter choice around  $\sin \theta = 0.1$  and  $v_\phi = 1000, 4000$  GeV are the most permissible choices to see the common parameter space for both the observed BAU and the Relic+DD+ID of Dark Matter. The observed Relic+DD+ID can be seen in Table.II.

As we mentioned earlier now we examine whether this model can provide a strong FOPT while sharing a common parameter space with both Leptogenesis and Dark Matter phenomenology. We have given 4 BPs in Table.III and the corresponding parameter space we get for the relic density of DM is under-abundant.

Among the 4 BPs provided in Table.III, the first two points do not satisfy the observed BAU and hence in the neighborhood of the parameter space of BP 1 and 2, BAU is over-abundant. The BPs 3 and 4 where the phase transition is along the BSM Higgs field direction are such that they satisfy the BAU and it can be studied in that parameter space and its neighborhood. From the results of our scan, we observed that the majority of the points show second-order

Parameters	$\sin \theta$	$M_{h_2}$ (GeV)	$v_\phi$ (GeV)	$\lambda_{H\Phi}$	$\eta_B$	$M_\chi$ (GeV)	$\Omega_\chi h^2$	$\sigma_{DD}^{SI}$ ( $cm^2$ )	$\langle \sigma v \rangle$ ( $cm^3/s$ )
1.	0.3	594.58	1000	0.3931	$6.1 \times 10^{-10}$	-	-	-	-
2.	0.3	594.18	4000	0.0981	$6.1 \times 10^{-10}$	154	0.11	$1.63 \times 10^{-47}$	$2.03 \times 10^{-26}$
3.	0.1	1128.31	1000	0.5086	$6.1 \times 10^{-10}$	137	0.11	$2.65 \times 10^{-47}$	$2.04 \times 10^{-26}$
4.	0.1	1129.41	4000	0.1274	$6.1 \times 10^{-10}$	873	0.11	$6.82 \times 10^{-47}$	$2.45 \times 10^{-26}$
5.	0.01	801.98	1000	0.0255	$3.1 \times 10^{-10}$	455	0.12	$2.91 \times 10^{-48}$	$2.51 \times 10^{-26}$
6.	0.01	802.02	4000	0.0064	$3.1 \times 10^{-10}$	355	0.09	$1.1 \times 10^{-49}$	$1.76 \times 10^{-27}$

TABLE II: *BAU allowed values compatible with the Relic + DD + ID parameter space.*

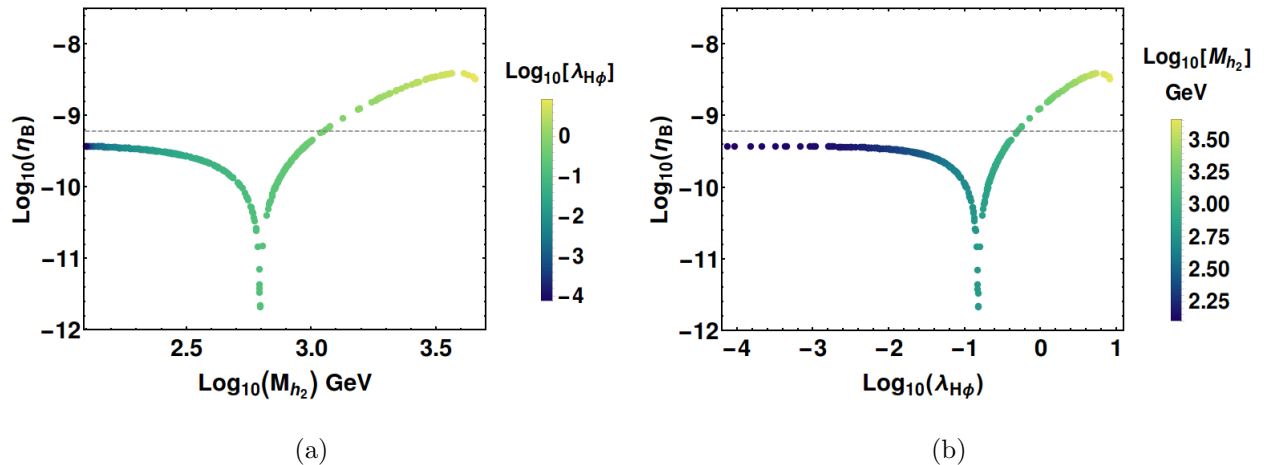


FIG. 15: *Figure shows the drop in the baryon asymmetry in the plane of  $M_{h_2}$ ,  $\lambda_{H\Phi}$  with the  $\eta_B$ . The horizontal Grey line represents the observed BAU.*

phase transition and those remaining points that show SFOPT along SM Higgs direction (or strong electroweak phase transition), the majority of them are ruled out by the latest LUXZEPLIN bound [84]. Corresponding to BP 1 and BP 2, the order parameter is greater than 1 along SM Higgs direction and less than 1 along BSM Higgs direction while corresponding to BP 3 and BP 4, the order parameter is greater than 1 along BSM Higgs direction and zero as there is no FOPT along SM Higgs direction. In Fig.16, different colors represent different phase transition phases. Color change with (without) an arrow indicates the possibility of a first (second) order phase transition. The black arrow corresponds to critical temperature and the brown arrow corresponds to nucleation temperature.

In Fig.16 (a) and (b), the phase structure of SM and BSM Higgs fields corresponding to BP 1 is shown as an example of Type A phase transition. From Fig.16, we see that there is a single step first order phase transition at the critical temperature  $T_c=107.71$  GeV along both

Parameters	BP 1	BP 2	BP 3	BP 4
$M_{h_2}$ (GeV)	1712.11	1542.39	398.11	400.16
$\sin \theta$	-0.34	-0.28	0.087	0.082
$v_\phi$ (GeV)	859.89	493.67	551.55	547.36
$M_\chi$ (GeV)	144.28	670.33	879.77	880.87
$\lambda_H$	2.915	1.735	0.138	0.137
$\lambda_{H\Phi}$	-4.408	-5.347	-0.092	0.088
$\lambda_\Phi$	1.758	4.789	0.682	0.697
$\mu_3$ (GeV)	-7.608	-286.054	-441.01	-445.51
$\Omega_\chi h^2$	$1.02 \times 10^{-2}$	$2.26 \times 10^{-5}$	$1.13 \times 10^{-2}$	$1.09 \times 10^{-2}$
$\sigma_{\text{DD}}^{\text{SI}}$ (cm <sup>2</sup> )	$3.48 \times 10^{-47}$	$3.59 \times 10^{-48}$	$2.125 \times 10^{-46}$	$1.86 \times 10^{-46}$
$\langle \sigma v \rangle^{\text{ID}}$ (cm <sup>3</sup> /s)	$6.4 \times 10^{-26}$	$5 \times 10^{-30}$	$2.35 \times 10^{-27}$	$2.27 \times 10^{-27}$
$\eta_B$	$5.66 \times 10^{-9}$	$3.95 \times 10^{-9}$	$2.29 \times 10^{-10}$	$2.36 \times 10^{-10}$

TABLE III: *Benchmark Points corresponding to SFOPT.*

the field directions. The transition is strong along SM Higgs direction with the value of order parameter  $\zeta_{c,1} = 1.105$ , and the transition is weak along BSM Higgs direction with the value of order parameter  $\zeta_{c,2} = 0.103$ . We represent a two step phase transition as an example of Type B phase transition in Fig.16 (c) and (d). The phase structure of both the SM and BSM Higgs fields are shown. In the first step, there is a phase transition along BSM Higgs field direction at the critical temperature  $T_c = 491.16$  GeV. In the second step, there is a second order phase transition in both the field directions. It would be extremely useful if we got to know the dependence of the different model parameters on the strength of the phase transition. For this purpose, we have shown the role of different model parameters on the strength of the phase transition along SM Higgs direction in Fig.17. The left panel of Fig.17 shows that with an increase of  $M_{h_2}$ , the phase transition strength increases, while we see the reverse effect for  $v_\phi$  in the right panel. The increase of  $M_{h_2}$  leads to the increase of the parameter  $\lambda_{H\Phi}$  from Eq.10. From Fig.14 (a), we see that such value of large  $\lambda_{H\Phi}$  is violating the BAU for a higher value of  $M_{h_2}$ . Thus we could not find any parameter space that satisfies SFOPT along SM Higgs direction (or SFOEWPT) along with the baryon asymmetry of the Universe. We still found a parameter space where both Leptogenesis and Dark Matter phenomenology along with SFOPT can be studied which is shown in Fig.14 (c) and (d). BP 3 and BP 4 of Table.III and their neighborhood fall in the common parameter space. The phase transition in that region is

Parameters	BP 1	BP 2	BP 3	BP 4
$T_c$	107.71	103	491.16	489.51
$(\langle h_1 \rangle, \langle h_2 \rangle) _{\text{High } T_c}$	(0, 813.74)	(0,454)	(0, 0)	(0, 0)
$(\langle h_1 \rangle, \langle h_2 \rangle) _{\text{Low } T_c}$	(119, 824.84)	(105,460)	(0, 502.9)	(0, 498.35)
$\zeta_c$	(1.105, 0.103)	(1.019, 0.058)	(0, 1.024)	(0, 1.018)
$T_n$	107.18	102.77	435.88	435.99
$(\langle h_1 \rangle, \langle h_2 \rangle) _{\text{High } T_n}$	(0, 813.74)	(0,454)	(0, 0)	(0, 0)
$(\langle h_1 \rangle, \langle h_2 \rangle) _{\text{Low } T_n}$	(129.32, 826.82)	(106,461)	(0, 522.68)	(0, 517.56)
$\alpha$	0.0129	0.0096	0.0045	0.0045
$\frac{\beta}{H}$	71453.3	146814	2677.4	2777.01

TABLE IV: Phase transition output parameters for SM and BSM Higgs directions corresponding to BPs. The values of high and low vevs ( $\langle h_1 \rangle, \langle h_2 \rangle$ ) of each of the scalar fields are given at all steps for all the benchmark points for both  $T_c$  and  $T_n$ . Temperature and vevs are in the GeV unit.

thus first order strong along the BSM Higgs field direction.

BP	DECIGO-corr	U-DECIGO	U-DECIGO-corr
1	-	-	$9.82 \times 10^6$
2	-	-	529167
3	10940.8	132912	$1.32 \times 10^8$
4	10287.2	126854	$1.26 \times 10^8$

TABLE V: SNR values corresponding to the Benchmark Points. The dashed lines indicate that the Gravitational wave spectrum associated with the benchmark point will not be detectable by the corresponding detector.

SFOPT leads to a background for the formation of stochastic Gravitational waves. The GW spectrum corresponding to the Benchmark Points are given in Fig.18 where the proposed sensitivities of the upcoming detectors U-DECIGO [36], U-DECIGO-corr [85] are depicted.

An important measure to detect the GW signal from its background is the SNR. We estimated the SNR values corresponding to all the BPs in Table.V using Eq.71. For the detection of GW in each relevant detector, the SNR value must exceed a threshold value for a particular setup. BP 1 and BP 2 SNRs in Table.V are less than the threshold value of DECIGO and U-DECIGO detectors. GW Spectrum corresponding to BP 3 and BP 4 can be detected in the DECIGO and U-DECIGO detectors. SNR values of BP 3 are higher than that of BP 4 as from

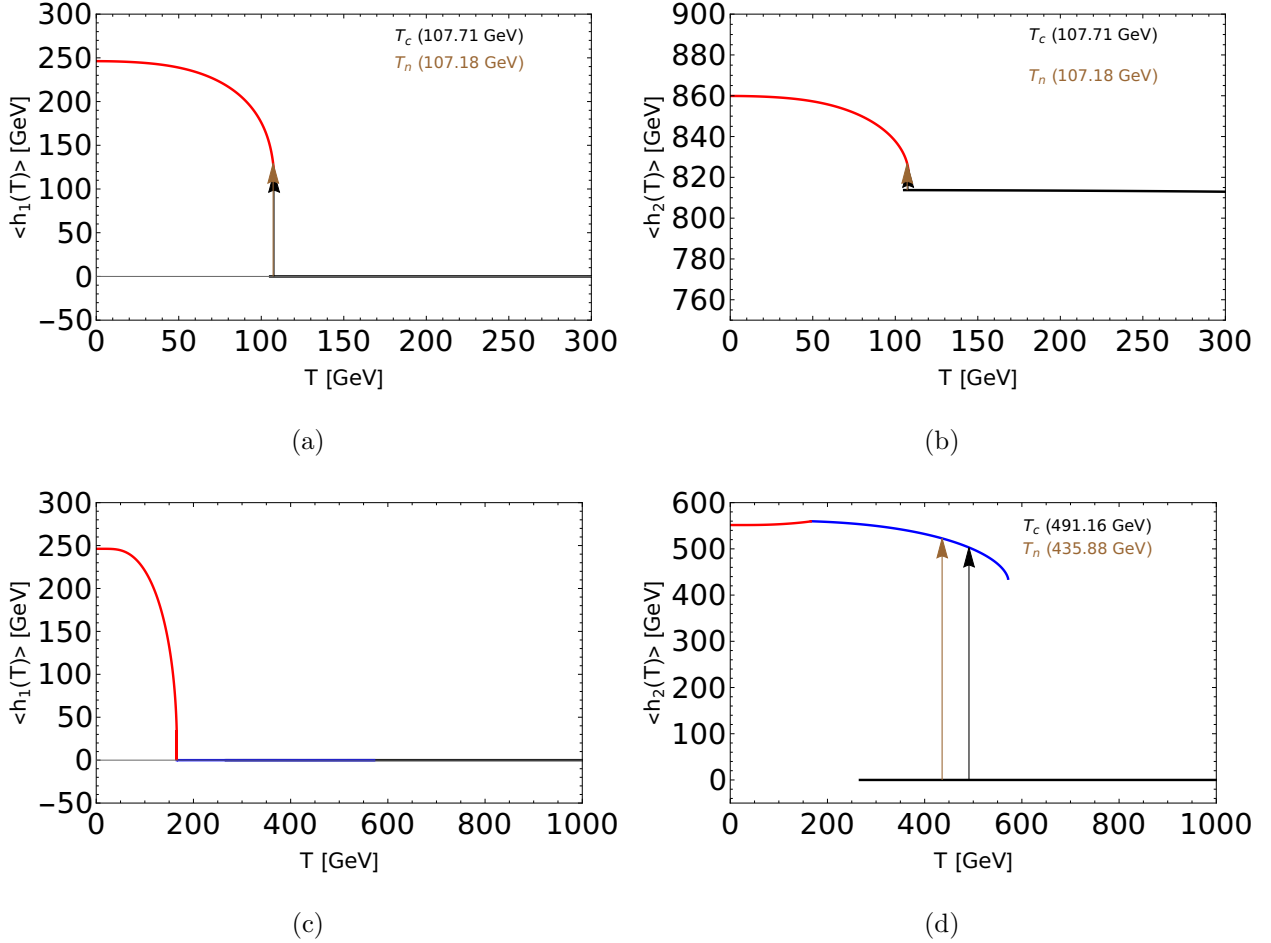


FIG. 16: (a), (b) represents the Phase Structure of the fields corresponding to BP 1, and (c), (d) represents the Phase Structure of the fields corresponding to BP 3.

Table.IV we can see that the order parameter  $\zeta_c$  of BP 3 is always higher than that of BP 4 resulting in greater signal strength.

## VII. SUMMARY AND CONCLUSION

Even though the Standard Model is a successful theory of fundamental particles and their interactions, it fails to explain the observed baryon symmetry of the Universe. Leptogenesis is an attractive mechanism to explain the observed baryon symmetry of the Universe. In standard thermal Leptogenesis, the Type-I seesaw model demands the mass of the right-handed neutrino to be very heavy which is hard to probe at low energy experimental setups. We considered an interesting scenario extending the Standard Model particle content with a singlet scalar to probe the Leptogenesis at a low scale. The singlet scalar couples with the right-handed neutrino pair which enables enhancing the additional CP-violation while attaining the observed BAU at low scale. Here we attempted to examine the allowed parameter space of the relic density of DM without adding an extra particle content but with the simple extension of the SM symmetry.

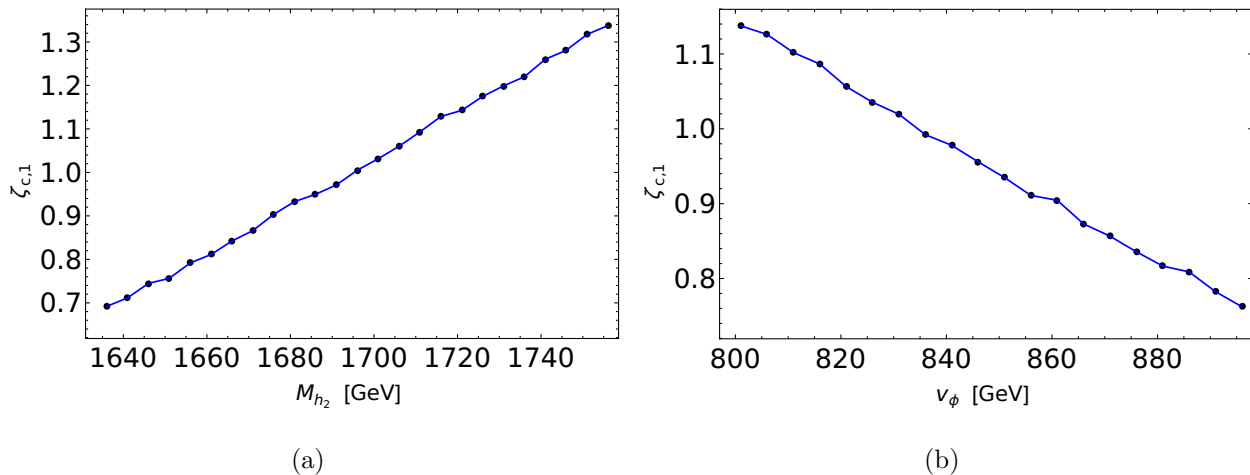


FIG. 17: *The role of a few model parameters in determining the Phase Transition strength along SM Higgs field direction. We have utilised the BP 1 for the purpose. Dots represent the exact value of order parameter obtained at the respective input variable.*

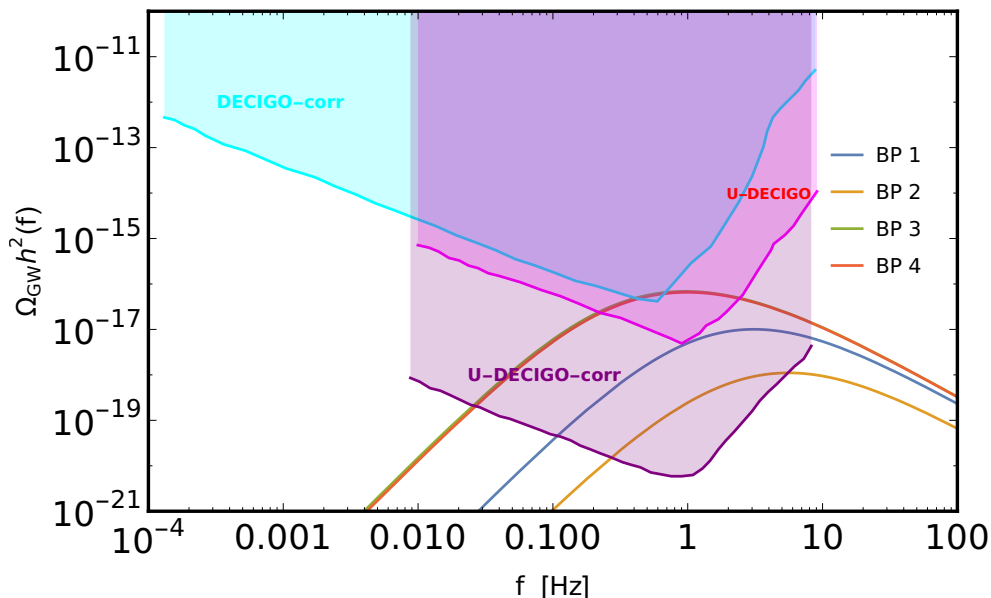


FIG. 18: *Gravitational Wave Spectrum corresponding to all the BPs 1-4.*

To fulfill these requirements, we consider the singlet complex scalar  $\Phi$  with an extended discrete symmetry  $\mathcal{Z}_3$ . The  $\mathcal{Z}_3$  allows a pair of  $\Phi$  to couple with right-handed neutrinos via a dimension-5 operator. After  $\Phi$  obtains a vacuum expectation value the CP-even part of the scalar, *i.e.*  $\phi$ , couples with the right-handed neutrinos  $N_i$ , ( $i = 1, 2$ ) through a Yukawa term. When the heavy right-handed neutrino  $N_2$  goes out of equilibrium and decays it generates the  $B-L$  asymmetry. In the presence of additional couplings, where  $N_2$  decays to  $N_1$  and  $\phi$ , *i.e.*,  $N_2 \rightarrow N_1 + \phi$ , which enhances the CP-violation and the corresponding lepton asymmetry compared to the standard leptogenesis scenario. However, the  $N_1$  generated lepton asymmetry is suppressed at a low energy  $\lesssim \mathcal{O}(10^6)$  GeV. The final  $B-L$  asymmetry transfers to the baryon asymmetry via the

EW sphaleron processes. On the other hand, the CP-odd part of the scalar  $\chi$  acts as a Pseudo scalar Dark Matter candidate due to a remnant  $\mathcal{Z}_2$ -like symmetry. The annihilation cross-section of the Pseudo scalar Dark Matter to the Standard Model particles through scalar-Higgs mixing can provide the observed relic density of the Dark Matter. Apart from probing BAU at a low scale satisfying all constraints of DM phenomenology, we also examined the possibility of SFOPT. SFOPT in our model is facilitated even at the tree level due to the presence of cubic terms in the potential. As the parameter space is already severely constrained from dark matter direct searches, we didn't get any point showing SFOPT along SM Higgs field which have correct relic density. Considering under-abundant relic density, we see that SFOPT along SM Higgs field direction violates BAU. SFOPT in the common parameter space still has under-abundant DM relic density and is along BSM Higgs field direction. Furthermore, SFOPTs generate a stochastic Gravitational Wave background which we examined corresponding to some benchmark points.

We have shown a common parameter space that can account for the universe's matter-antimatter asymmetry and is consistent with low-energy neutrino data through the Casas-Ibarra parametrization. Furthermore, this parameter space can explain the observed relic density of dark matter while satisfying constraints from direct and indirect dark matter searches, including those by XENON-1T, LZ 2022, Fermi-LAT, and MAGIC *etc.* Our final observations are displayed in the plane of  $\lambda_{H\Phi} - M_{h_2}$  for a fixed set of values. For the parameter choice we consider indicating that the  $\sin\theta = 0.1$  and  $v_\phi = 1000, 4000$  GeV are more appropriate parameter regions to look for the observed BAU and Dark Matter simultaneously. We have shown four benchmark points where a strong FOPT is possible. Among the four benchmark points, two benchmark points fall in the order of the observed BAU *i.e.*,  $\mathcal{O}(10^{-10})$  and with the corresponding relic density under-abundant,  $\mathcal{O}(10^{-2})$ . We have shown the future detection perspective of Gravitational Wave signals corresponding to four benchmark points that fall in the detection sensitivity of the DECIGO-corr, U-DECIGO, and U-DECIGO-corr. To enhance the compatibility of strong first-order phase transitions (SFOPT) with both baryon asymmetry of the universe (BAU) and dark matter (DM) constraints, a more comprehensive exploration of the model parameter space is needed.

## Acknowledgments

KM would like to thank Nandini Das for valuable discussions and acknowledges the financial support provided by the Indian Association for the Cultivation of Science (IACS), Kolkata. PG gratefully acknowledges the support from IACS, Kolkata, India, where most of this work was carried out.

## VIII. APPENDICES

### A. Vertex factors

Following are the vertex factors for vertices relevant to the calculation of the Relic density of Dark Matter given in Figs.5, 6,

$$\begin{aligned}
h_1\chi\chi &: -\frac{3\mu_3 \sin\theta}{\sqrt{2}} - \lambda_{H\Phi}v \cos\theta + 2\lambda_\Phi v_\phi \sin\theta \approx \frac{\sin\theta (M_{h_1}^2 + \frac{4}{3}M_\chi^2)}{v_\phi}, \\
h_2\chi\chi &: \frac{3\mu_3 \cos\theta}{\sqrt{2}} - \lambda_{H\Phi}v \sin\theta - 2\lambda_\Phi v_\phi \cos\theta \approx -\frac{\cos\theta (M_{h_2}^2 + \frac{4}{3}M_\chi^2)}{v_\phi}, \\
h_1h_1\chi\chi &: -2\lambda_\Phi \sin^2\theta - \lambda_{H\Phi} \cos^2\theta \approx -\frac{(M_{h_2}^2 - M_{h_1}^2) \sin\theta}{v v_\phi}, \\
h_1h_2\chi\chi &: 2\lambda_\Phi \sin\theta \cos\theta - \lambda_{H\Phi} \sin\theta \cos\theta \\
&\approx \frac{\sin\theta (3v_\phi \sin\theta (M_{h_1}^2 - M_{h_2}^2) + v (3M_{h_2}^2 + M_\chi^2))}{3v v_\phi^2}, \\
h_2h_2\chi\chi &: \frac{1}{2} (-2\lambda_\Phi \cos^2\theta - \lambda_{H\Phi} \sin^2\theta) \approx -\frac{3M_{h_2}^2 + M_\chi^2}{3v_\phi^2}. \tag{72}
\end{aligned}$$

### B. Loop functions

Following are the loop function parameters discussed in Sec.III for the CP-asymmetry diagrams<sup>5</sup>,

$$F_{ij,R}^{(v)} = \sqrt{r_{ji}} \ln \left[ \frac{(1 - r_{ji}) - (\sigma_i + \sqrt{\delta_{ji}})}{(1 - r_{ji}) - (\sigma_i - \sqrt{\delta_{ji}})} \right], \tag{73}$$

$$F_{ij,L}^{(v)} = -\sqrt{\delta_{ji}} + r_{ji} \ln \left[ \frac{(1 - r_{ji}) - (\sigma_i + \sqrt{\delta_{ji}})}{(1 - r_{ji}) - (\sigma_i - \sqrt{\delta_{ji}})} \right], \tag{74}$$

$$F_{ijk,RR}^{(s)} = \frac{\sqrt{r_{ji}}\sqrt{r_{ki}}\sqrt{\delta_{ji}}}{1 - r_{ji}}, \quad F_{ijk,RL}^{(s)} = \frac{1}{2} \frac{\sqrt{r_{ki}}\sqrt{\delta_{ji}}(1 + r_{ji} - \sigma_i)}{1 - r_{ji}}, \tag{75}$$

$$F_{ijk,LL}^{(s)} = \frac{\sqrt{r_{ji}}\sqrt{\delta_{ji}}}{1 - r_{ji}}, \quad F_{ijk,LR}^{(s)} = \frac{1}{2} \frac{\sqrt{\delta_{ji}}(1 + r_{ji} - \sigma_i)}{1 - r_{ji}}. \tag{76}$$

Where  $r_{ij} \equiv M_i^2/M_j^2$ ,  $\sigma_i \equiv M_\Phi^2/M_i^2$  and  $\delta_{ij} \equiv (1 - r_{ij} - \sigma_j)^2 - 4r_{ij}\sigma_j$ .

<sup>5</sup> Note that before EWSB, the zero temperature SM Higgs mass is considered massless.

### C. Zero Temperature Counter Terms

Following are the expressions of all the counter terms corresponding to each parameter that appears in the tree-level potential:

$$\begin{aligned}
\delta\lambda_H &= \frac{1}{2v^3}(\partial_h\Delta V - v\partial_h^2\Delta V), & \delta\lambda_\Phi &= \frac{1}{2v_\phi^3}(\partial_\phi\Delta V - v_\phi\partial_\phi^2\Delta V), \\
\delta\lambda_{H\Phi} &= -\frac{\partial_h\partial_\phi\Delta V}{vv_\phi}, & \delta\mu_3 &= 0, \\
\delta\mu_H^2 &= \frac{1}{2v}(3\partial_h\Delta V - v_\phi\partial_h\partial_\phi\Delta V - v\partial_h^2\Delta V), \\
\delta\mu_\Phi^2 &= \frac{1}{2v_\phi}(3\partial_\phi\Delta V - v\partial_\phi\partial_h\Delta V - v_\phi\partial_\phi^2\Delta V),
\end{aligned} \tag{77}$$

where all the derivatives are evaluated at  $h = v$  and  $\phi = v_\phi$ .

- 
- [1] PLANCK collaboration, N. Aghanim et al., *Planck 2018 results. VI. Cosmological parameters*, *Astron. Astrophys.* **641** (2020) A6, [[1807.06209](#)].
  - [2] A. D. Sakharov, *Violation of CP Invariance, C asymmetry, and baryon asymmetry of the universe*, *Pisma Zh. Eksp. Teor. Fiz.* **5** (1967) 32–35.
  - [3] V. A. Rubakov and M. E. Shaposhnikov, *Electroweak baryon number non-conservation in the early universe and in high-energy collisions*, *Physics-Uspekhi* **39** (May, 1996) 461–502.
  - [4] A. Mazumdar and G. White, *Review of cosmic phase transitions: their significance and experimental signatures*, *Reports on Progress in Physics* **82** (June, 2019) 076901.
  - [5] M. Fukugita and T. Yanagida, *Baryogenesis Without Grand Unification*, *Phys. Lett. B* **174** (1986) 45–47.
  - [6] V. A. Kuzmin, V. A. Rubakov and M. E. Shaposhnikov, *On the Anomalous Electroweak Baryon Number Nonconservation in the Early Universe*, *Phys. Lett. B* **155** (1985) 36.
  - [7] SNO collaboration, Q. R. Ahmad et al., *Direct evidence for neutrino flavor transformation from neutral current interactions in the Sudbury Neutrino Observatory*, *Phys. Rev. Lett.* **89** (2002) 011301, [[nucl-ex/0204008](#)].
  - [8] J. N. Bahcall and C. Pena-Garay, *Solar models and solar neutrino oscillations*, *New J. Phys.* **6** (2004) 63, [[hep-ph/0404061](#)].
  - [9] SUPER-KAMIOKANDE collaboration, S. Fukuda et al., *Constraints on neutrino oscillations using 1258 days of Super-Kamiokande solar neutrino data*, *Phys. Rev. Lett.* **86** (2001) 5656–5660, [[hep-ex/0103033](#)].

- [10] KAMLAND collaboration, K. Eguchi et al., *First results from KamLAND: Evidence for reactor anti-neutrino disappearance*, *Phys. Rev. Lett.* **90** (2003) 021802, [[hep-ex/0212021](#)].
- [11] P. Minkowski,  $\mu \rightarrow e\gamma$  at a Rate of One Out of  $10^9$  Muon Decays?, *Phys. Lett. B* **67** (1977) 421–428.
- [12] T. Yanagida, *Horizontal gauge symmetry and masses of neutrinos*, *Conf. Proc. C* **7902131** (1979) 95–99.
- [13] R. N. Mohapatra and G. Senjanovic, *Neutrino Mass and Spontaneous Parity Nonconservation*, *Phys. Rev. Lett.* **44** (1980) 912.
- [14] F. Zwicky, *Die Rotverschiebung von extragalaktischen Nebeln*, *Helv. Phys. Acta* **6** (1933) 110–127.
- [15] V. C. Rubin and W. K. Ford, Jr., *Rotation of the Andromeda Nebula from a Spectroscopic Survey of Emission Regions*, *Astrophys. J.* **159** (1970) 379–403.
- [16] W. Hu and S. Dodelson, *Cosmic Microwave Background Anisotropies*, *Ann. Rev. Astron. Astrophys.* **40** (2002) 171–216, [[astro-ph/0110414](#)].
- [17] E. W. Kolb and M. S. Turner, *The Early Universe*, vol. 69. 1990, [10.1201/9780429492860](#).
- [18] XENON collaboration, E. Aprile et al., *Dark Matter Search Results from a One Ton-Year Exposure of XENON1T*, *Phys. Rev. Lett.* **121** (2018) 111302, [[1805.12562](#)].
- [19] PANDAX-4T collaboration, Y. Meng et al., *Dark Matter Search Results from the PandaX-4T Commissioning Run*, *Phys. Rev. Lett.* **127** (2021) 261802, [[2107.13438](#)].
- [20] LZ collaboration, J. Aalbers et al., *First Dark Matter Search Results from the LUX-ZEPLIN (LZ) Experiment*, [2207.03764](#).
- [21] FERMI-LAT collaboration, M. Ackermann et al., *Searching for Dark Matter Annihilation from Milky Way Dwarf Spheroidal Galaxies with Six Years of Fermi Large Area Telescope Data*, *Phys. Rev. Lett.* **115** (2015) 231301, [[1503.02641](#)].
- [22] MAGIC, FERMI-LAT collaboration, M. L. Ahnen et al., *Limits to Dark Matter Annihilation Cross-Section from a Combined Analysis of MAGIC and Fermi-LAT Observations of Dwarf Satellite Galaxies*, *JCAP* **02** (2016) 039, [[1601.06590](#)].
- [23] F. Kahlhoefer, *Review of LHC Dark Matter Searches*, *Int. J. Mod. Phys. A* **32** (2017) 1730006, [[1702.02430](#)].
- [24] E. K. Akhmedov, V. A. Rubakov and A. Y. Smirnov, *Baryogenesis via neutrino oscillations*, *Phys. Rev. Lett.* **81** (1998) 1359–1362, [[hep-ph/9803255](#)].
- [25] A. Pilaftsis and T. E. J. Underwood, *Resonant leptogenesis*, *Nucl. Phys. B* **692** (2004) 303–345, [[hep-ph/0309342](#)].
- [26] T. Hugle, M. Platscher and K. Schmitz, *Low-Scale Leptogenesis in the Scotogenic Neutrino*

- Mass Model*, *Phys. Rev. D* **98** (2018) 023020, [[1804.09660](#)].
- [27] E. Ma, *Verifiable radiative seesaw mechanism of neutrino mass and dark matter*, *Phys. Rev. D* **73** (2006) 077301, [[hep-ph/0601225](#)].
- [28] T. Alanne, T. Hugle, M. Platscher and K. Schmitz, *Low-scale leptogenesis assisted by a real scalar singlet*, *JCAP* **03** (2019) 037, [[1812.04421](#)].
- [29] M. Le Dall and A. Ritz, *Leptogenesis and the Higgs Portal*, *Phys. Rev. D* **90** (2014) 096002, [[1408.2498](#)].
- [30] J. A. Casas and A. Ibarra, *Oscillating neutrinos and  $\mu \rightarrow e, \gamma$* , *Nucl. Phys. B* **618** (2001) 171–204, [[hep-ph/0103065](#)].
- [31] S. Davidson and A. Ibarra, *A Lower bound on the right-handed neutrino mass from leptogenesis*, *Phys. Lett. B* **535** (2002) 25–32, [[hep-ph/0202239](#)].
- [32] G. Engelhard, Y. Grossman, E. Nardi and Y. Nir, *The Importance of  $N_2$  leptogenesis*, *Phys. Rev. Lett.* **99** (2007) 081802, [[hep-ph/0612187](#)].
- [33] B. P. Abbott, R. Abbott, R. Adhikari, P. Ajith, B. Allen, G. Allen et al., *Ligo: the laser interferometer gravitational-wave observatory*, *Reports on Progress in Physics* **72** (June, 2009) 076901.
- [34] P. Amaro-Seoane, H. Audley, S. Babak, J. Baker, E. Barausse, P. Bender et al., *Laser interferometer space antenna*, 2017.
- [35] J. Crowder and N. J. Cornish, *Beyond lisa: Exploring future gravitational wave missions*, *Physical Review D* **72** (Oct., 2005) .
- [36] H. Kudoh, A. Taruya, T. Hiramatsu and Y. Himemoto, *Detecting a gravitational-wave background with next-generation space interferometers*, *Phys. Rev. D* **73** (Mar, 2006) 064006.
- [37] Z. Kang, P. Ko and T. Matsui, *Strong first order ewpt  $\mathcal{E}$  strong gravitational waves in  $z\beta$ -symmetric singlet scalar extension*, *Journal of High Energy Physics* **2018** (Feb., 2018) .
- [38] K. Kannike, K. Loos and M. Raidal, *Gravitational wave signals of pseudo-Goldstone dark matter in the  $\mathbb{Z}_3$  complex singlet model*, *Phys. Rev. D* **101** (2020) 035001, [[1907.13136](#)].
- [39] C. Gross, O. Lebedev and T. Toma, *Cancellation Mechanism for Dark-Matter–Nucleon Interaction*, *Phys. Rev. Lett.* **119** (2017) 191801, [[1708.02253](#)].
- [40] J. Chakraborty, P. Konar and T. Mondal, *Copositive Criteria and Boundedness of the Scalar Potential*, *Phys. Rev. D* **89** (2014) 095008, [[1311.5666](#)].
- [41] J. Horejsi and M. Kladiva, *Tree-unitarity bounds for THDM Higgs masses revisited*, *Eur. Phys. J. C* **46** (2006) 81–91, [[hep-ph/0510154](#)].
- [42] ATLAS collaboration, G. Aad et al., *A detailed map of Higgs boson interactions by the ATLAS experiment ten years after the discovery*, *Nature* **607** (2022) 52–59, [[2207.00092](#)].

- [43] CMS collaboration, A. Tumasyan et al., *A portrait of the Higgs boson by the CMS experiment ten years after the discovery.*, *Nature* **607** (2022) 60–68, [[2207.00043](#)].
- [44] S. D. Lane, I. M. Lewis and M. Sullivan, *Resonant Multi-Scalar Production in the Generic Complex Singlet Model in the Multi-TeV Region*, [2403.18003](#).
- [45] D. López-Val and T. Robens,  *$\Delta r$  and the  $W$ -boson mass in the singlet extension of the standard model*, *Phys. Rev. D* **90** (2014) 114018, [[1406.1043](#)].
- [46] ATLAS collaboration, G. Aad et al., *Constraints on new phenomena via Higgs boson couplings and invisible decays with the ATLAS detector*, *JHEP* **11** (2015) 206, [[1509.00672](#)].
- [47] P. F. de Salas, D. V. Forero, S. Gariazzo, P. Martínez-Miravé, O. Mena, C. A. Ternes et al., *2020 global reassessment of the neutrino oscillation picture*, *JHEP* **02** (2021) 071, [[2006.11237](#)].
- [48] I. Esteban, M. C. Gonzalez-Garcia, M. Maltoni, T. Schwetz and A. Zhou, *The fate of hints: updated global analysis of three-flavor neutrino oscillations*, *JHEP* **09** (2020) 178, [[2007.14792](#)].
- [49] W. Buchmuller, P. Di Bari and M. Plumacher, *Leptogenesis for pedestrians*, *Annals Phys.* **315** (2005) 305–351, [[hep-ph/0401240](#)].
- [50] S. Bhattacharya, P. Poulose and P. Ghosh, *Multipartite Interacting Scalar Dark Matter in the light of updated LUX data*, *JCAP* **04** (2017) 043, [[1607.08461](#)].
- [51] G. Bélanger, F. Boudjema, A. Pukhov and A. Semenov, *micromegas4.1: Two dark matter candidates*, *Computer Physics Communications* **192** (July, 2015) 322–329.
- [52] A. Alloul, N. D. Christensen, C. Degrande, C. Duhr and B. Fuks, *Feynrules 2.0 — a complete toolbox for tree-level phenomenology*, *Computer Physics Communications* **185** (Aug., 2014) 2250–2300.
- [53] P. Ghosh, A. K. Saha and A. Sil, *Study of Electroweak Vacuum Stability from Extended Higgs Portal of Dark Matter and Neutrinos*, *Phys. Rev. D* **97** (2018) 075034, [[1706.04931](#)].
- [54] J. M. Alarcon, L. S. Geng, J. Martin Camalich and J. A. Oller, *The strangeness content of the nucleon from effective field theory and phenomenology*, *Phys. Lett. B* **730** (2014) 342–346, [[1209.2870](#)].
- [55] S. Coleman and E. Weinberg, *Radiative corrections as the origin of spontaneous symmetry breaking*, *Phys. Rev. D* **7** (Mar, 1973) 1888–1910.
- [56] L. Dolan and R. Jackiw, *Symmetry behavior at finite temperature*, *Phys. Rev. D* **9** (Jun, 1974) 3320–3341.
- [57] M. Quiros, *Finite temperature field theory and phase transitions*, in *ICTP Summer School in High-Energy Physics and Cosmology*, pp. 187–259, 1, 1999. [hep-ph/9901312](#).
- [58] R. R. Parwani, *Resummation in a hot scalar field theory*, *Phys. Rev. D* **45** (1992) 4695, [[hep-ph/9204216](#)].

- [59] M. Quirós, *On daisy and superdaisy resummation of the effective potential at finite temperature*, 1993.
- [60] H. H. Patel and M. J. Ramsey-Musolf, *Baryon Washout, Electroweak Phase Transition, and Perturbation Theory*, *JHEP* **07** (2011) 029, [[1101.4665](#)].
- [61] M. Laine, *Gauge dependence of the high-temperature two-loop effective potential for the higgs field*, *Physical Review D* **51** (Apr., 1995) 4525–4532.
- [62] M. Garny and T. Konstandin, *On the gauge dependence of vacuum transitions at finite temperature*, *Journal of High Energy Physics* **2012** (July, 2012) .
- [63] J. Espinosa, M. Garny, T. Konstandin and A. Riotto, *Gauge-independent scales related to the standard model vacuum instability*, *Physical Review D* **95** (Mar., 2017) .
- [64] N. Nielsen, *On the gauge dependence of spontaneous symmetry breaking in gauge theories*, *Nuclear Physics B* **101** (1975) 173–188.
- [65] R. Fukuda and T. Kugo, *Gauge invariance in the effective action and potential*, *Phys. Rev. D* **13** (Jun, 1976) 3469–3484.
- [66] C. L. Wainwright, *Cosmotransitions: Computing cosmological phase transition temperatures and bubble profiles with multiple fields*, *Computer Physics Communications* **183** (Sept., 2012) 2006–2013.
- [67] C. Grojean and G. Servant, *Gravitational waves from phase transitions at the electroweak scale and beyond*, *Physical Review D* **75** (Feb., 2007) .
- [68] *Decay of the false vacuum at finite temperature: A. linde, nucl. phys. b216 (1983) 421*, *Nuclear Physics B* **223** (1983) 544.
- [69] A. Linde, *On the vacuum instability and the higgs meson mass*, *Physics Letters B* **70** (1977) 306–308.
- [70] I. Affleck, *Quantum-statistical metastability*, *Phys. Rev. Lett.* **46** (Feb, 1981) 388–391.
- [71] C. Caprini, M. Hindmarsh, S. Huber, T. Konstandin, J. Kozaczuk, G. Nardini et al., *Science with the space-based interferometer elisa. ii: gravitational waves from cosmological phase transitions*, *Journal of Cosmology and Astroparticle Physics* **2016** (Apr., 2016) 001–001.
- [72] J. Ellis, M. Lewicki and J. M. No, *Gravitational waves from first-order cosmological phase transitions: lifetime of the sound wave source*, *Journal of Cosmology and Astroparticle Physics* **2020** (July, 2020) 050–050.
- [73] M. Kamionkowski, A. Kosowsky and M. S. Turner, *Gravitational radiation from first-order phase transitions*, *Phys. Rev. D* **49** (Mar, 1994) 2837–2851.
- [74] J. Kehayias and S. Profumo, *Semi-analytic calculation of the gravitational wave signal from the electroweak phase transition for general quartic scalar effective potentials*, *Journal of Cosmology*

*and Astroparticle Physics* **2010** (Mar., 2010) 003–003.

- [75] A. Nicolis, *Relic gravitational waves from colliding bubbles and cosmic turbulence*, *Classical and Quantum Gravity* **21** (Jan., 2004) L27–L33.
- [76] R. Jinno and M. Takimoto, *Gravitational waves from bubble collisions: An analytic derivation*, *Physical Review D* **95** (Jan., 2017) .
- [77] P. Borah, P. Ghosh, S. Roy and A. K. Saha, *Electroweak phase transition in a right-handed neutrino superfield extended NMSSM*, *JHEP* **08** (2023) 029, [2301.05061].
- [78] M. Hindmarsh, S. J. Huber, K. Rummukainen and D. J. Weir, *Gravitational waves from the sound of a first order phase transition*, *Physical Review Letters* **112** (Jan., 2014) .
- [79] M. Hindmarsh, *Sound shell model for acoustic gravitational wave production at a first-order phase transition in the early universe*, *Physical Review Letters* **120** (Feb., 2018) .
- [80] M. Hindmarsh, S. J. Huber, K. Rummukainen and D. J. Weir, *Shape of the acoustic gravitational wave power spectrum from a first order phase transition*, *Phys. Rev. D* **96** (2017) 103520, [1704.05871].
- [81] H.-K. Guo, K. Sinha, D. Vagie and G. White, *Phase transitions in an expanding universe: stochastic gravitational waves in standard and non-standard histories*, *Journal of Cosmology and Astroparticle Physics* **2021** (Jan., 2021) 001–001.
- [82] C. Caprini, R. Durrer and G. Servant, *The stochastic gravitational wave background from turbulence and magnetic fields generated by a first-order phase transition*, *Journal of Cosmology and Astroparticle Physics* **2009** (Dec., 2009) 024–024.
- [83] K. Kuroda, W.-T. Ni and W.-P. Pan, *Gravitational waves: Classification, methods of detection, sensitivities and sources*, *International Journal of Modern Physics D* **24** (Dec., 2015) 1530031.
- [84] LZ collaboration, J. Aalbers et al., *First Dark Matter Search Results from the LUX-ZEPLIN (LZ) Experiment*, *Phys. Rev. Lett.* **131** (2023) 041002, [2207.03764].
- [85] K. Yagi and N. Seto, *Detector configuration of decigo/bbo and identification of cosmological neutron-star binaries*, *Physical Review D* **83** (Feb., 2011) .